AFRL-IF-RS-TR-2003-270
Final Technical Report
November 2003

COMPUTER MICROVISION FOR MICROELECTROMECHANICAL SYSTEMS (MEMS)

Massachusetts Institute of Technology

Sponsored by
Defense Advanced Research Projects Agency
DARPA Order No. E117

APPROVED FOR PUBLIC RELEASE; DISTRIBUTION UNLIMITED.

AIR FORCE RESEARCH LABORATORY
INFORMATION DIRECTORATE
ROME RESEARCH SITE
ROME, NEW YORK

STINFO FINAL REPORT

This report has been reviewed by the Air Force Research Laboratory, Information Directorate, Public Affairs Office (IFOIPA) and is releasable to the National Technical Information Service (NTIS). At NTIS it will be releasable to the general public, including foreign nations.

AFRL-IF-RS-TR-2003-270 has been reviewed and is approved for publication

/s/

APPROVED:

DANIEL J. BURNS
Project Engineer

FOR THE DIRECTOR: /s/

JAMES A. COLLINS, Acting Chief
Information Technology Division
Information Directorate

REPORT DOCUMENTATION PAGE

Form Approved
OMB No. 074-0188

1. AGENCY USE ONLY (Leave blank)	2. REPORT DATE	3. REPORT TYPE AND DATES COVERED
	NOVEMBER 2003	Final May 97 – Jun 03

4. TITLE AND SUBTITLE
COMPUTER MICROVISION FOR MICROELECTROMECHANICAL SYSTEMS (MEMS)

5. FUNDING NUMBERS
C - F30602-97-2-0106
PE - 63739E
PR - E117
TA - 00
WU - 11

6. AUTHOR(S)
Dennis M. Freeman

7. PERFORMING ORGANIZATION NAME(S) AND ADDRESS(ES)
Massachusetts Institute of Technology
Cambridge Massachusetts 02139-4307

8. PERFORMING ORGANIZATION REPORT NUMBER
N/A

9. SPONSORING / MONITORING AGENCY NAME(S) AND ADDRESS(ES)
Defense Advanced Research Projects Agency
3701 North Fairfax Drive
Arlington Virginia 22203-1714

AFRL/IFTC
26 Electronic Parkway
Rome New York 13441-4514

10. SPONSORING / MONITORING AGENCY REPORT NUMBER
AFRL-IF-RS-TR-2003-270

11. SUPPLEMENTARY NOTES
AFRL Project Engineer: Daniel J. Burns/IFTC/(315) 330-2335/ Daniel.Burns@rl.af.mil

12a. DISTRIBUTION / AVAILABILITY STATEMENT
APPROVED FOR PUBLIC RELEASE; DISTRIBUTION UNLIMITED.

12b. DISTRIBUTION CODE

13. ABSTRACT *(Maximum 200 Words)*
This effort successfully addressed a critical need related to the early design and evaluation of Microelectromechanical systems (MEMS) by developing tools and methods for testing and characterizing MEMS devices that enabled in situ visualization of the motions of internal structures in MEMS by combining light microscopy, video imaging, and machine vision. A series of MEMS test bed platforms were developed under this project that used stroboscopic illumination to produce temporal sequences of images of microelectromechanical systems that were magnified with a microscope, projected onto a CCD camera, and recorded at multiple planes of focus. These images could be viewed at playback speeds chosen to facilitate human interpretation of the motions, and they could be analyzed using methods originally conceived for robot vision to determine quantitative device performance parameters. One platform was replicated at a number of major MEMS research Universities, and another was transitioned as a commercial product. A number of collaborations with MEMS developers provided critical measurements and functional MEMS performance evaluations. Additional work developed a patented multi-beam interferometric method for imaging MEMS, launched a collaborative Computer Microvision Remote Test Facility using DARPA's Next Generation Internet, and produced a high-end animation to communicate the complexity and importance of MEMS fabrication.

14. SUBJECT TERMS
Microvision Microelectromechanical Nanometer, Optical Characterization Test, Interferometry Stroboscopy Resonator Switch, Gyroscope Grating Mirror

15. NUMBER OF PAGES
54

16. PRICE CODE

17. SECURITY CLASSIFICATION OF REPORT	18. SECURITY CLASSIFICATION OF THIS PAGE	19. SECURITY CLASSIFICATION OF ABSTRACT	20. LIMITATION OF ABSTRACT
UNCLASSIFIED	UNCLASSIFIED	UNCLASSIFIED	UL

Table of Contents

1. Program Goals……..... 1

2. Major Accomplishments……..... 2

3. Description of Major Accomplishments…… 3
3.1. Computer microvision platforms…… 3
3.1.1. Zeiss Axioplan Platform……. 3
3.1.1.1. Video microscopy…… 3
3.1.1.2. Stroboscopic illumination…… 4
3.1.1.3. Modular stimulus generator……..... 4
3.1.1.4. Motion estimates from video images……... 4
3.1.1.5. 3D measurements……..... 5
3.1.2 Benchtop Platform……..... 6
3.1.3 Turnkey Platform……..... 7
3.1.4 Modular Computer Microvision System……..……..... 7
3.1.5 Linnik Interferometric Platform……11
3.1.6 Mirau Interferometric Platform……..... 13

3.2 Collaborations with MEMS Developers……...17
3.2.1. Modal Analysis of microfabricated gyroscope……17
3.2.2. Calibration of fatigue test structure……. 20
3.2.3. Resonance analysis of 3D motion sensors…….. 23
3.2.4. Characterization of CMOS MEMS……. 25
3.2.5. Displacements of optical gratings……27
3.2.6. Alignment of optical switches…..…… 29
3.2.7. Modal analysis of LIGA fail-safe device…… 30
3.2.7.1. Substrate motions…… 31
3.2.7.2. Shuttle motions…… 31
3.2.7.3. Detailed analysis of motions at 650Hz…… 33

3.3. Multi-beam interferometric optical imaging for MEMS…….…... 35
3.3.1. Experimental verification of theory..……..…… 35
3.3.2. Summary…….…….…….. 36

3.4 Matisse..…….. 38

3.5 Envisioning MEMS, A Communications Initiative …..……..40

Publications……..…..….47

References……..47

List of Figures

Figure 1. Computer Vision measurement system……. 3
Figure 2. Stroboscopic, volumetric imaging……. 4
Figure 3. Turn-on and turn-off times of the LED……. 5
Figure 4. Benchtop Computer Microvision Hardware …… 6
Figure 5. Modular Computer Microvision Imaging System…… 7
Figure 6. Turnkey Platform with Real-Time Display…….. 8
Figure 7. Measurement and analysis packages…… 9
Figure 8. Viewer……. 9
Figure 9. Reports……. 9
Figure 10. Supporting data ……. 10
Figure 11. Virtual lab notebook ..…… 10
Figure 12. Optical table setup for Interferometric Computer Microvision…….. 11
Figure 13. Zeiss Mirau interferometer……. 13
Figure 14. Brightfield and Mirau Interferometric images of a lateral resonator..... 14
Figure 15. In-plane displacements…… 15
Figure 16. Out-of-plane displacements……. 16
Figure 17. Computer microvision image of a microfabricated gyroscope developed by The Charles Stark Draper Laboratory…….. 17
Figure 18. Modes of motion of the Draper gyroscope…….. 18
Figure 19. Modal decomposition for other stimulus conditions……... 19
Figure 20. Microfabricated test structure from Exponent Failure Analysis Associates, Inc…… 20
Figure 21. Accuracy of rotation estimates…… 21
Figure 22. Calibration of a fatigue test structure…….. 21
Figure 23. Three dimensional rotations of fatigue test structure…….. 22
Figure 24. Gyroscope developed by Wyatt Owen Davis at the Berkeley Sensors and Actuators Center..……... 23
Figure 25. Displacement amplitude frequency response of BSAC gyroscope with sinusoidal stimulus of 10 Volts DC plus 5 Volts AC …… 24
Figure 26. Displacement amplitude frequency response of BSAC gyroscope with a sinusoidal stimulus of 20 Volts DC plus 10 Volts AC…… 24
Figure 27. CMU MEMS gyroscope device…….. 25
Figure 28. Frequency response of MEMS gyroscope……... 26
Figure 29. MEMS optical grating……. 27
Figure 30. Out-of-plane positions of grating elements……. 28
Figure 31. Three-dimensional image of the microfabricated mirror and its reflection in the substrate…… 29
Figure 32. Orientation and analysis of motions of “Device B”…… 30
Figure 33. Driven substrate motions ..…….. 31
Figure 34. Shuttle motions…… 32
Figure 35. Measured motion amplitudes of the shuttle at 650Hz ……33
Figure 36. A multi-beam interferometric microscope experimental setup……36
Figure 37. Processed data from the setup in Figure 36 …… 37
Figure 38. Network of Computer Microvision measurement sites……... 39
Figure 39. Selected Images from supplemental discs……... 41

List of Figures (cont.)

Figure 40. More selected images from supplemental discs……. 41
Figure 41. More selected images from supplemental discs…….. 42
Figure 42. More selected images from supplemental discs…….. 43
Figure 43. Animation sequence images - manufacturing……. 45
Figure 44. Animation sequence images - elements……... 45
Figure 45.Animation sequence images – reaction…… 46

1. PROGRAM GOALS

Microelectromechanical systems (MEMS) are manufactured using batch fabrication techniques that are similar to those used to manufacture microelectronic devices. Unlike electronics, however, simple methods for testing and characterizing internal failure modes of micromechanical devices do not exist. This limitation has important consequences for designers and fabricators of MEMS. For the designer, it can result in large numbers of costly prototypes. For the fabricator, it means reduced yields because common techniques such as laser trimming cannot be applied. As the demand for precision micromechanical parts increases, and as the complexity of microelectromechanical systems increases, developing better tools for characterizing the performance of MEMS becomes crucial.

The major goal of the proposed work is

- **to develop inexpensive and reliable tools**
- **for in situ visualization of the motions of internal structures in MEMS**
- **by combining light microscopy, video imaging, and machine vision.**

Images of microelectromechanical systems will be magnified with a microscope and projected onto a CCD camera. Stroboscopic illumination will be used to take temporal sequences of images at multiple planes of focus. Recorded images can then be viewed at playback speeds chosen to facilitate human interpretation of the motions. Quantitative estimates of motions will also be obtained directly from the recorded images using algorithms originally conceived for robot vision.

2. MAJOR ACCOMPLISHMENTS

- Developed a series of Computer Microvision Platforms for motion analysis of MEMS:
  - Zeiss Axioplan Platform: high quality commercial optics plus custom electronics; 3 units installed and in use, one at MIT, one at the Berkeley Sensors and Actuators Center, and one at Carnegie Mellon University.
  - Benchtop Platform: low-cost custom optics and modular electronics. Provides superior light performance and mechanical stability than commercial microscope systems and therefore makes measurements faster.
  - Turnkey Platform: prototype system for commercialization. Commercial product now available from Umech Technologies LLC. (Watertown, MA) — marking successful transition to commercial sector.
  - Linnik Interferometric Platform: prototype interferometric system with improved axial resolution and larger field of view than comparable brightfield system.
  - Mirau Interferometric Platform: off-the-shelf commercial interference objective with pre-aligned optical path lengths makes interferometric measurements as simple to make as brightfield measurements.
- Demonstrated the use of Computer Microvision in real-world applications in collaborations with MEMS developers:
  - Modal analysis of microfabricated gyroscope (The Charles Stark Draper Laboratory)
  - Calibration of a fatigue test structure (Exponent Failure Analysis Associates, Inc.)
  - Resonance analysis of 3D motion sensors (Berkeley Sensors and Actuators Center)
  - Characterization of CMOS MEMS (Carnegie Mellon University (CMU))
  - Displacements of optical gratings (City Univ. of New York (CUNY) at Albany)
  - Alignment of optical switches (University of California in Los Angeles (UCLA))
  - Modal analysis of LIGA fail-safe device (Naval Surface Warfare Center, Indian Head Division)
- Developed a novel, multi-beam interferometric optical approach for imaging MEMS.
  - Patented through MIT's Technology Licensing Office
  - Provided the basis for two follow-on DARPA contracts (Synthetic Aperture Lithography and Synthetic Aperture Metrology)
- Launched Matisse, a collaborative project to develop a Computer Microvision Remote Test Facility using DARPA's Next Generation Internet.
  - Collaborative effort with the Center for National Research Initiatives (CNRI), the University of California at Berkeley (Berkeley), Carnegie Mellon University (CMU), Lawrence Berkeley National Laboratory (LBNL), and Sarnoff Corp.
  - Provide remote access to Computer Microvision test stations at MIT, Berkeley, and CMU using Next Generation Internet technologies.
- Envisioning MEMS, A Communications Initiative. Under the direction of Felice Frankel, The Envisioning MEMS effort has created a high-end animation (See labeled CD: ENVISIONING MEMS) to communicate the complexity and importance of MEMS fabrication in a clear, concise, and compelling fashion.

3. DESCRIPTION OF MAJOR ACCOMPLISHMENTS

3.1 Computer Microvision Platforms

3.1.1 Zeiss Axioplan Platform

We developed a high quality Computer Microvision Platform based on a commercial optical microscope, commercial camera, and custom electronics. The commercial components were optimized for high precision and high resolution measurements. The custom electronics provided an arbitrary periodic signal for stimulating the MEMS, synchronized stroboscopic illumination, and external signals to synchronize with the camera.

Three identical platforms were constructed. They were located at MIT, Berkeley Sensors and Actuators Center, and Carnegie Mellon University, where there are all still in use.

3.1.1.1 Video microscopy. Test structures are mounted on the stage of a light microscope (Zeiss Axioplan 2 Motorized Research Microscope, Oberkochen, Germany). Objectives (Zeiss LD-Epiplan 20$\times$ and 50$\times$) are chosen to achieve high resolution (numerical apertures are 0.4 and 0.6, respectively) with sufficient working distance (9.8 mm and 3.5 mm, respectively) to accommodate external electrical probes. The objectives are attached to the microscope through a piezoelectric focusing unit (PIFOC, Polytec PI, Waldbronn, Germany) to provide precise control of axial position. Magnified images are projected onto a CCD camera (Pulnix TM-1010), which has 1024 $\times$ 1024 pixels with 9 μm spacing. Digitized images from the camera are communicated to a Pentium based computer using a frame grabber (Imaging Technology).

Figure 1: Computer Microvision measurement system. MEMS are positioned on the stage of a microscope (left) that has been modified for 3D stroboscopic imaging by (1) replacing the halogen lamp with an LED, (2) mounting the microscope objective on a piezoelectric focusing unit (controller shown in top center), and (3) attaching a CCD camera (top left). A computer controls a modular stimulus generator (bottom center) which provides two synchronized waveforms: one to drive motions of the MEMS and one to pulse the LED for stroboscopic illumination.

3.1.1.2 Stroboscopic illumination. The maximum frame rate of a digital video imager is typically on the order of tens of Hertz. To image faster motions, we use stroboscopic illumination. A green LED (Nichia NSPG500S, Tokushima 774, Japan) is pulsed so that the target is illuminated at a selected phase of its motion (see waveforms in Figure 2). Light from the LED is collected with a halogen lamp housing: the halogen lamp was removed, and the LED was mounted near the intended position of the tungsten filament. The plastic lens that originally covered the LED's die was milled away and the flat surface was polished, so that illumination was Köhler [7].

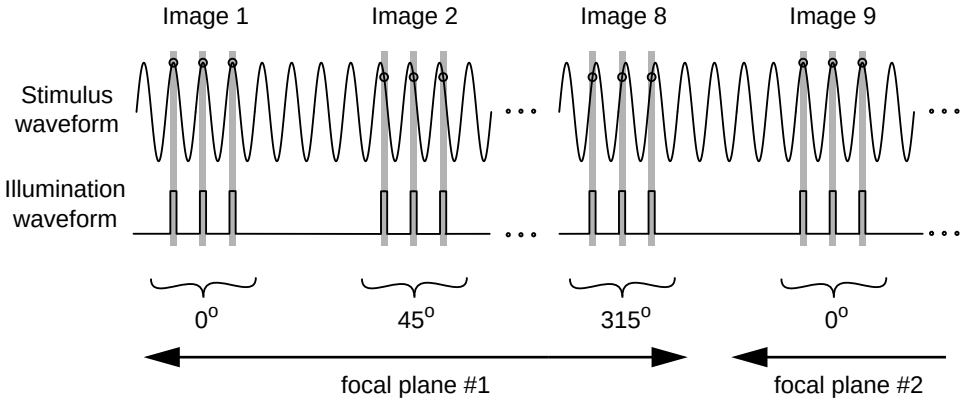

Figure 2: Stroboscopic, volumetric imaging. Motions are driven with a periodic stimulus. The first image is acquired when light from the LED samples the image at times corresponding to peaks in the stimulus waveform. Successive images are acquired at different phases. This process is then repeated for different focal planes selected by a computer-controlled focus adjustment.

3.1.1.3 Modular stimulus generator. A single 5"×10" printed circuit card (Figure 1) contains all of the circuitry needed to produce the stimulus and timing waveforms for Computer Microvision (Figure 2). The card contains a high speed 12-bit DAC (Analog Devices AD9713) and a static memory chip (64 K bytes by 16 bits) that is used to hold one cycle of an arbitrary periodic stimulus. The period of the stimulus can be controlled to generate rates from 1 Hz to 1 MHz with mHz resolution.

The modular stimulus generator also controls the stroboscopic illumination. The amplitude, turn-on time, and turn-off time are under program control. The stimulus generator can be programmed to sample any number of phases per stimulus period, and arbitrary waits can be programmed to allow transients to decay between stimulus presentations. Stroboscopic illumination can be synchronized to the internally generated stimulus or it can be synchronized to external clocks, which is important for measuring devices that are self-clocked.

Since the intensity of the light emitted from an LED is more nearly proportional to current than voltage, the LED is driven by a computer-controlled D/A converter via a voltage-to-current converter. Pulsing is accomplished by switching the current to the LED on and off with a high-speed transistor (ZVN3306A). Because LEDs are fast, the shortest light pulse (Figure 3) is limited in practice by the electronics driving the LED (roughly 100 ns for our circuit). Thus, the stroboscopic sampling rate can be as high as 5 MHz.

3.1.1.4 Motion estimates from video images. To characterize sinusoidal motions, eight or

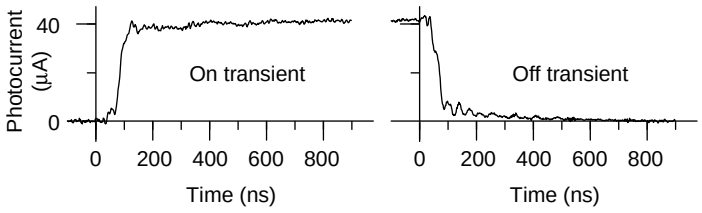

Figure 3: Turn-on and turn-off times of the LED. The signal to the LED was turned on (left) and off (right) and light from the LED was measured using a high-speed photodiode (Motorola MRD500). The traces show the averages of 200 transients.

sixteen images of the specimen are acquired at evenly-spaced phases of the stimulus cycle using stroboscopic illumination. The LED is gated so that the duty cycle is 1/8 period if eight images are collected or 1/16 period if 16 phases are collected.

Displacements between images acquired at successive phases are estimated directly from the video images. Although image resolution is limited by the optics [6] to distances on the order of the wavelength of light (typically 525 nm), displacements between two such images as small as nanometers can be reliably measured [3]. Algorithms for motion detection are described elsewhere [2, 8].

3.1.1.5 3D measurements. Silicon devices are opaque to green light. Nevertheless, information about axial motion can be obtained from images obtained from different focal planes. Images from above the best plane of focus of a structure are blurred. As the structure moves axially, the axial blurring pattern moves with the structure. Therefore, the algorithms that are used to track in-plane motions by computing in-plane gradients can equally track out-of-plane motions by computing out-of-plane gradients [8]. Images are acquired at different focal planes to obtain information about 3D motion. In early experiments, focus was adjusted by translating the stage in the axial direction using an integrated stepper motor (part of the Zeiss Axioplan 2 Motorized Research Microscope). This method provided axial positioning with 0.1 μm resolution over large axial excursions — essentially limited only by the rack-and-pinion mechanism that supported the stage. However, axial motions were accompanied by submicrometer in-plane displacements. In later experiments, focus was controlled by translating the objective with a piezoelectric crystal (PIFOC, Polytec PI, Wandbronn, Germany). Although this device limited the maximum axial excursion to 100 μm, in-plane displacements were significantly smaller.

3.1.2 Benchtop Platform

We have designed and constructed a benchtop tube microscope system for MEMS measurements (Figure 4). The system is assembled almost entirely from commercial off-the-shelf components, and is intended to provide high stability, ease of replication and flexible deployment, ease of adjustment and interchange of parts, and compatibility with systems built around laboratory microscopes, at a reasonable cost. The 150 mm optical path can accept a variety of both standard and high quality (e.g., Zeiss) objectives. Precision Newport stages provide full X-Y-Z positioning to accommodate a variety of devices and can be equipped with manual or motorized actuators. A mini X-Y-Z stage is used for convenient positioning of the LED light source. Only three components require machining: the plastic body of the LED is machined flat and polished to optimize its use as a light source in a microscope (exactly as we do in our Zeiss system), an aluminum LED holder, and an optional steel plate for fixing device platforms to the vertical stage with magnets. The system is assembled on a small optical platform (TMC 19" x 23" base). The small "footprint" of this system makes it usable in a small laboratory space or even an office. When necessary, this system can be moved as a unit and placed on a vibration isolation table for high precision measurements. In comparison to the Zeiss microscope system, the benchtop tube system provides superior light (and hence, faster test times) and mechanical stability, at some cost in reduced features and flexibility. The system is used with exactly the same computer hardware and modular stimulator (XPOZ 2.2) that is used with our Zeiss platforms.

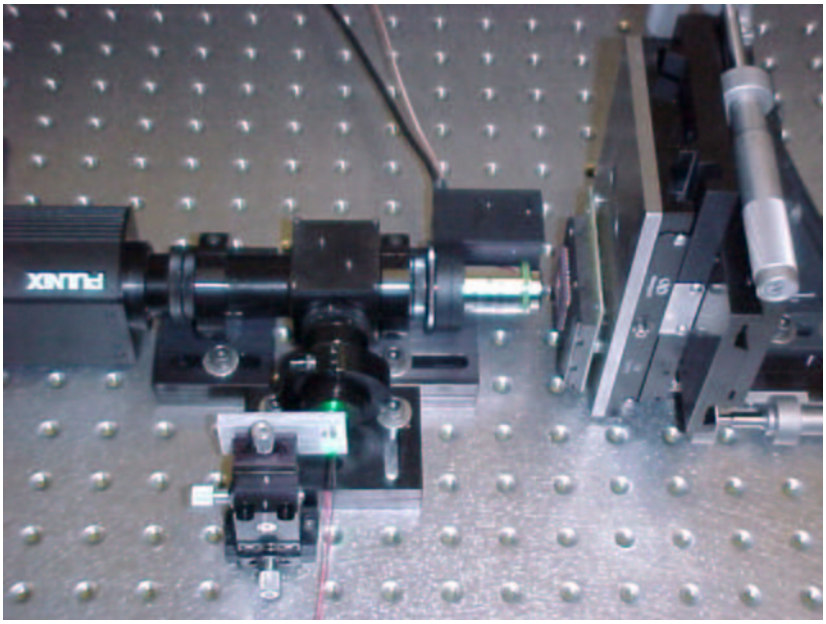

Figure 4: Benchtop Computer Microvision Hardware. Except for the microscope and stage, this system uses the same hardware (camera, piezoelectric focus control, stimulus and illumination) and software as the Zeiss-based system, at significantly lower cost.

3.1.3 Turnkey Platform

We have developed a Turnkey Platform to demonstrate the feasibility of constructing a commercial Computer Microvision System. The hardware is optimized to be simple and inexpensive. The software is optimized to be user friendly, to facilitate the use of the platform with a minimum of detailed knowledge about optics and video microscopy. Following our demonstration of this platform, Umech Technologies, LLC, has developed and is now selling a Computer Microvision Workstation commercially.

3.1.4 Modular Computer Microvision System We have developed a modular Computer Microvision imaging system that combines the waveform generation and stroboscopic illumination features of our modular arbitrary waveform generator (XPOZ 2.2) with a CCD imaging chip. The new system uses a single field programmable logic array (FPGA) to coordinate all critical timing, including MEMS stimulus generation, stroboscopic illumination, and imaging. This eliminates synchronization problems that arise when the camera, illuminator, and waveform generator are separate units. The FPGA is part of Anapolis Microsystems Wild-One, a high-speed digital interface that communicates to a Pentium-based computer via the PCI bus. In combination with an optical microscope, this system provides all of the hardware required for two-dimensional motion measurements of MEMS. With the addition of a focusing element (such as Polytec PI's PIFOC), the system will perform full 3D motion analysis.

The system uses a Texas Instruments TC237 CCD imaging chip, which provides 640×480 pixel images at a maximum refresh rate of 30 Hz. The output is digitized with a 10-bit analog to digital (A/D) converter (Analog Devices AD9050). Digital to analog converters (AD9760) are provided for arbitrary waveform generation. Complete analog circuitry is also provided for stroboscopic illumination with an LED. The amplifiers and strobe cards plug into a general purpose bus (Figure 5). Multiple amplifiers and strobe cards can be combined to tailor the system to particular needs. We have used the unit to stimulate motions of MEMS as high as 100 kHz and obtained high quality images at rates as high as 20 per second.

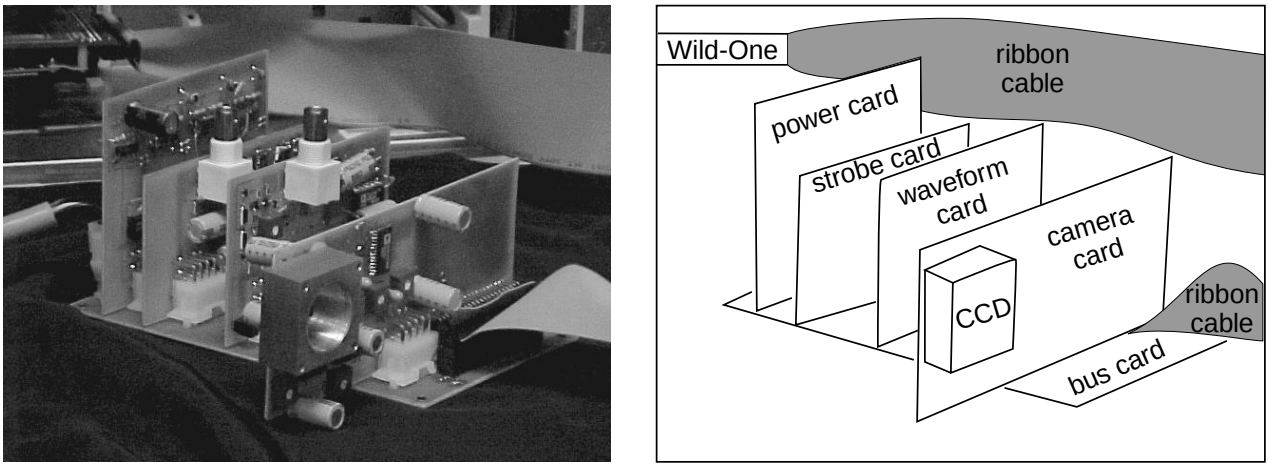

Figure 5: Modular Computer Microvision Imaging System

We have developed an integrated, turnkey metrology station for MEMS (Figure 6). The station combines our benchtop tube microscope and modular computer microvision imaging system with

Web-based control software that simplifies making measurements — so that users can focus on their MEMS, not on programming. The user places a device on the measurement stage and connects the stimulus generator (using a zero-insertion-force socket or probes). On power-up, a flat-panel display automatically shows real-time video images of the MEMS. The 20 Hz refresh rate is optimized to facilitate positioning and focusing of the video microscope using an integrated 3D translation stage.

The modular stimulus generator can be configured for 0 to 7 channels that each produce an arbitrary, periodic signal that is synchronized to the stroboscopic illuminator. Each channel is controlled by a 12-bit digital-to-analog converter with a 13 MHz sampling rate. The associated amplifiers produce full-amplitude (-20 V to 20 V) signals with more than 100 kHz bandwidth. Frequencies can be controlled with sub-tenth-Hz resolution. The stroboscopic illuminator uses a high performance LED (Nichia NSPG500S) to turn the light on or off in less than 100 ns, allowing stop-action imaging of megahertz motions.

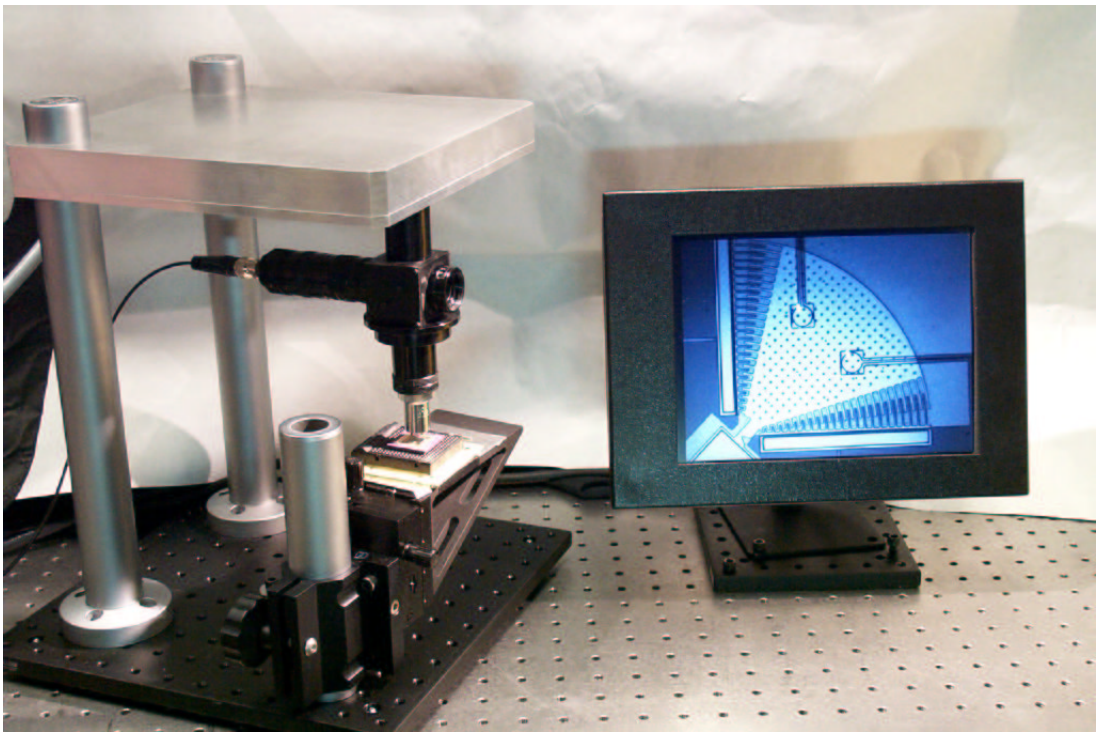

Figure 6: Turnkey Platform with Real-Time Display. Real-time video images of the MEMS on the measurement platform are displayed with a 20 Hz refresh rate to facilitate positioning and focusing. All other aspects of measurement are controlled via a Web browser.

Except for positioning the MEMS on the measurement stage and connecting the stimulus generator to the part, all operations are controlled from a Web browser. This interface provides the ultimate in cross-platform compatibility. Any internet-capable platform can control the measurement system using a Java-capable Web browser (such as Netscape 4.7). Control via the internet also allows remote control. Measurement stations in remote locations, such as clean rooms, can be completely controlled from your office or from anywhere.

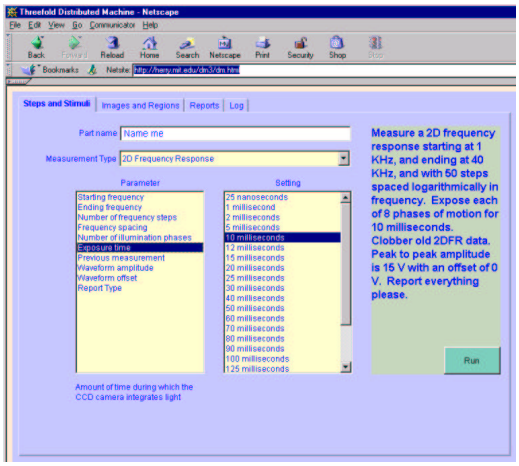

Figure 7: Measurement and analysis packages. Measurement and analysis protocols, such as Snapshot and 2D Frequency Response, are selected from a pull-down menu labeled Measurement Type. Parameters of the selected measurement type are chosen from the left column and then their values are selected from the right column. Short help messages associated with each parameter and value automatically appear beneath each column. The right box contains a summary statement of the measurement as it is currently configured. This statement provides a quick way to verify that all parameters are set properly without having to click through all of the settings. Clicking Run initiates the measurement.

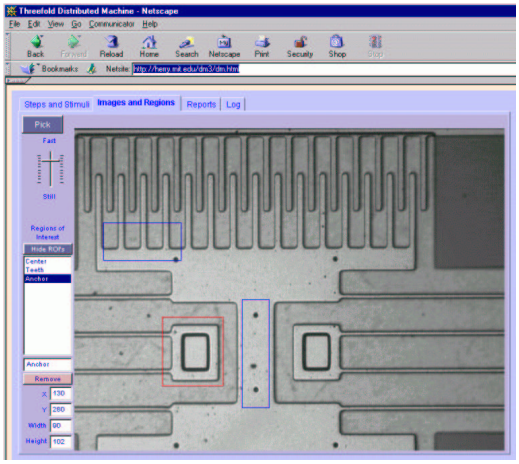

Figure 8: Viewer. Images that are recorded during any measurement can be viewed as still shots. Arbitrary sequences of images can be viewed as slow-motion video clips. Regions of interest (ROIs) for subsequent analysis can be selected and named.

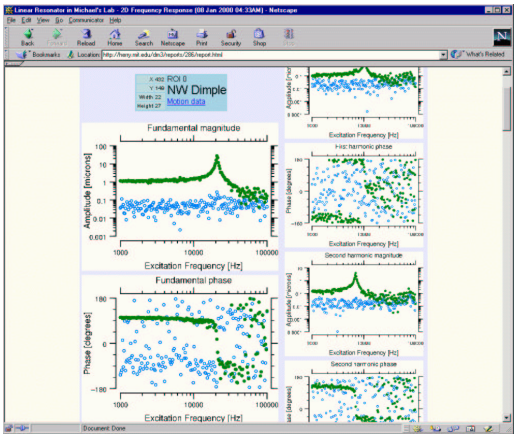

Figure 9: Reports. When measurements are completed, a report is automatically generated. This panel shows the first page of the report for a 2D Frequency Response. The plots show frequency responses for the part of the MEMS inside the first ROI. Similar pages are produced for all other ROIs. The frequency responses show the magnitudes and angles of the fundamental component of motion in the x (blue) and y (green) directions. Similar plots also show the magnitudes and angles of the first 3 harmonics. Clicking on a plot automatically generates a window that contains the numbers that are plotted, for easy incorporation of results into spreadsheets and text processors.

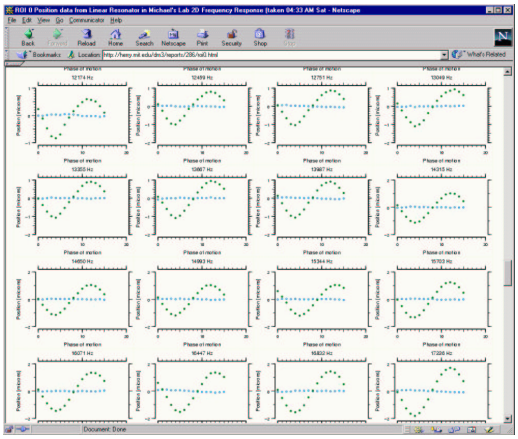

Figure 10: Supporting data. While the first page of the report provides a summary of results from a measurement, subsequent pages show the supporting data. For a 2D Frequency Response, the supporting data include time traces for motions measured at each frequency and for each ROI. As with all plots, the numbers that are plotted can be accessed by simply clicking the plot panel.

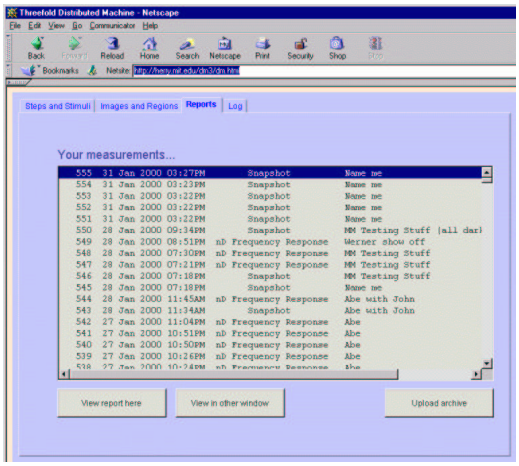

Figure 11: Virtual lab notebook. Every measurement is time-stamped, logged, and saved for future reference. Clicking on a measurement allows users to view the report for that measurement. Since reports from previous measurements are always saved, the user can confidently make a variety of measurements, compare results, and then Upload the most relevant ones later. Upload causes the entire report (main pages plus supporting pages) to be saved into a “zip” file that is transfered from the measurement station to the user’s computer (which is running the network browser). The zip file is compatible with all common platforms (Windows, Apple, and Unix) and provides a local copy of complete report.

3.1.5 Linnik Interferometric Platform

To demonstrate the use of interferometric methods to measure motions, we developed a Linnik Interferometic Computer Microvision Platform. The interferometric microscope is configured much like a Michelson interferometer with the addition of 2 microscope objectives. Light from a high-performance LED is broken into two paths by a beam-splitter. Light in one path is focused onto a MEMS target using a 20X microscope objective. Light in the other path is focused by a similar 20X objective onto a reference mirror, whose axial position is controlled with a piezoelectric actuator. Reflected beams from both paths are recombined and interfere with each other in the coincident back-focal planes of the objectives, where images are acquired with a CCD camera.

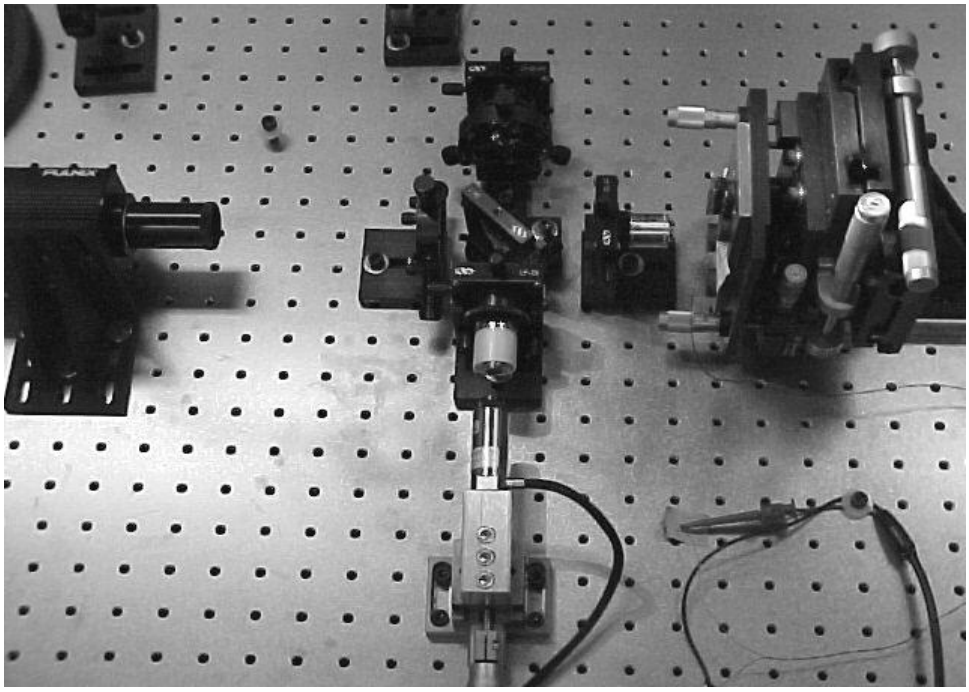

Figure 12: Optical table setup for Interferometric Computer Microvision

Although light from an LED has a short coherence length (on the order of tens of micrometers), it was possible to adjust the relative lengths of the two arms of the interferometer to produce images with high-contrast interference fringes. For every stimulus condition of the MEMS target (excitation amplitude, frequency, and stroboscopic phase), a sequence of interferograms is collected for different axial positions of the reference mirror. Every pixel in the sequence collects an intensity that, in the absence of optical imperfections and noise, would vary approximately sinusoidally with the optical phase of the reference mirror. The amplitude of that sinusoidal variation is proportional to the intensity in a brightfield image, and is thus suitable for in-plane analysis using Computer Microvision. The phase of the sinusoidal intensity variation encodes the relative out-of-plane position of the surface at the target. Thus, by estimating both the magnitude and phase of the intensities of each pixel observed in a sequence of piezo voltages, we extract sufficient information for full 3D motion estimation.

We compared the performance of Interferometric Computer Microvision with Brightfield

Computer Microvision, and results are contained in a manuscript that has been published [5]. For comparable systems (i.e., same microscope objective) and comparable amount of averaging (i.e., same number of images) measurements with Interferometric Computer Microvision have significantly higher axial resolution than do those with Brightfield Computer Microvision. This result can be understood by considering the basic physical mechanisms that limit axial resolution in these systems. Axial resolution in Brightfield Computer Microvision depends on axial contrast in 3D brightfield images, and axial contrast depends heavily on the numerical aperture of the objective. Axial resolution in Interferometric Computer Microvision depends on an interference phenomenon that is insensitive to numerical aperture. This insensitivity means that Interferometric Computer Microvision can use lower numerical aperture objectives, which can offer a number of important advantages.

- Field of view. Generally, high numerical aperture can only be achieved for objectives with high magnifications. The higher the magnification, the smaller the field of view, given the same camera. Since the interference system allows the use of lower numerical apertures than brightfield, it also affords greater fields of view for comparable out-of-plane sensitivity.
- Long working-distance. Generally, high numerical aperture can only be achieved for objectives with short working distances. Since the interference system allows the use of lower numerical apertures than does brightfield, it can achieve the same out-of-plane sensitivities using objectives with longer working distances. Increasing working-distance simplifies the integration of the measurement system with other experimental apparatus such as electrical probes and vacuum systems.
- Size of data set. The lower magnifications used with Interferometric Computer Microvision result in smaller datasets: typically more than an order of magnitude smaller for comparable motion resolution. Smaller data sets require smaller amounts of disk storage, and even more significantly, allow the measurements to be taken much more rapidly.

Although the interference system has many advantages over brightfield, there are also disadvantages. For example, precise adjustment of the two optical paths is difficult. Furthermore, the high out-of-plane sensitivity makes the system very sensitive to unintended motions, such as those caused by table vibrations and drift in the piezo-electric actuator.

3.1.6 Mirau Interferometric Platform

We have developed a Mirau interferometric video system for measuring three-dimensional motions of MEMS with nanometer resolution. We had previously demonstrated a Linnik interferometric imaging system (previous section) that used custom-fabricated optics, which were difficult and time-consuming to align. The Mirau interferometric system is based on commercial optics that are aligned by the manufacturer and provides out-of-plane resolution comparable to the Linnik interferometer.

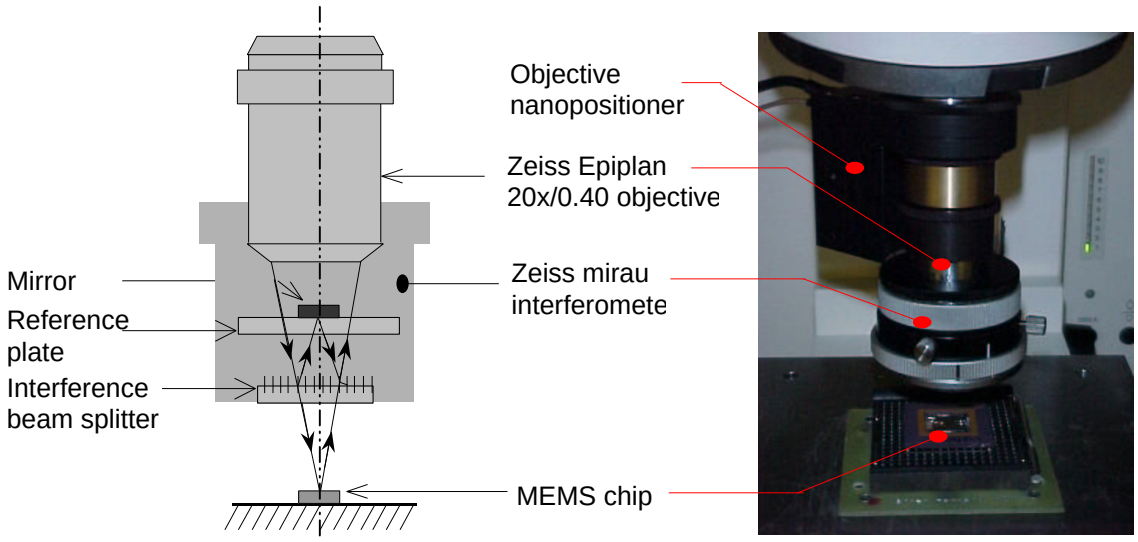

Figure 13: Zeiss Mirau interferometer. Left: Schematic representation. Illumination from the objective is split into two parts by a beam splitter. One part reflects off the MEMS chip and the other part reflects off a mirror on the reference plate. The two parts combine and interfere. Right: Photograph. The Zeiss Mirau interferometer is attached to the microscope through a nanopositioner that translates the interferometer axially.

The Mirau interferometer (Zeiss Corporation, Germany) consists of a beamsplitter and reference mirror that are packaged into a single unit (Figure 13, right panel) that mounts directly on a long working-distance objective (Zeiss LD-Epiplan 20x). Control knobs allow fine adjustment of the relative optical path lengths. Furthermore, the reference mirror can be rotated out of the beam path so that both brightfield and interference images can be obtained. The Mirau interferometer is attached to the microscope turret via an objective nanopositioner (P720, PIFOC, Polytec PI, Germany). Motions of the nanopositioner alter the optical path length to the target relative to the optical path length to the reference mirror. Interferograms obtained at multiple positions of the nanopositioner are analyzed to determine axial motions of the target in terms of known displacements of the nanopositioner.

Stroboscopic illumination is used to take stop-action interferograms and stop-action brightfield images at multiple phases of periodically driven motions of the MEMS device under test. Illumination is generated using an array of seven LEDs (C505-CB290-E1000, Cree Research Inc., USA). The fast optical rise time of the LEDs (30 ns) allows stop action motion analysis at frequencies up to tens of MHz. The optical bandwidth (50 nm centered at l = 505 nm) produces light with a coherence length of approximately 15 μm. Thus, interferometric data can be obtained from structures with heights within a 7 μm range. The stroboscopic interferograms were analyzed

to determine out-of-plane (z) displacement. The brightfield images were analyzed to determine in-plane (x and y) displacement. Thus the combination of stroboscopic interferograms and brightfield images allows three-dimensional motion analysis.

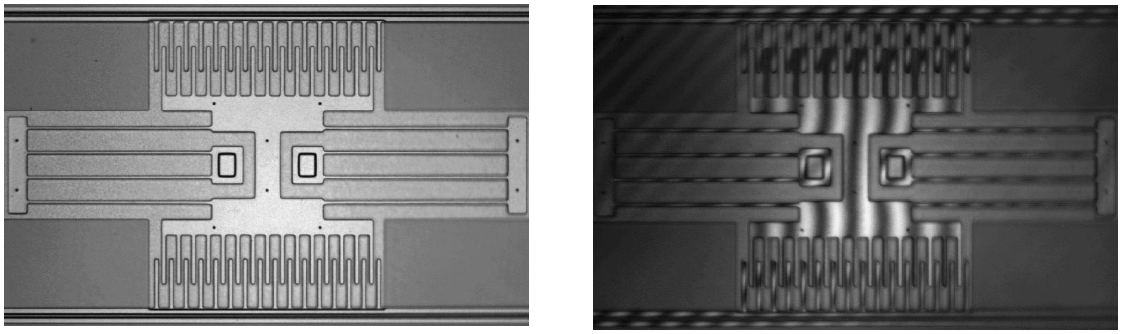

Figure 14: Brightfield and Mirau Interferometric images of a lateral resonator. Both images were obtained using the apparatus described in Figure 13. The brightfield image (left) was obtained with the reference mirror rotated out of the optical path. The interferometic image (right) was obtained with the reference mirror rotated into the optical path.

To demonstrate the motion measurement system, a surface micromachined lateral resonator (fabricated with the MUMPs process, Cronos Integrated Microsystems, USA) was electrically stimulated with a sinusoidal voltage (10 Vp-p AC plus 50 V DC bias) applied to one of the comb drives and the shuttle mass was connected to ground. The system was placed on a vibration isolation table and in an enclosure to minimize the effects of external vibrations and air currents. Brightfield images and interferograms (Figure 14) were obtained at 8 evenly spaced phases of motion and recorded with a CCD camera (Pulnix 1010, Pulnix Inc., USA). For three-dimensional intereferometric analysis, interferograms at nine planes of focus (separated by 30 nm) and one brightfield image (at the plane of best focus) were obtained for 8 stimulus phases at each of 33 frequencies (from 1 kHz to 50 kHz).

For three-dimensional brightfield analysis, brightfield images at 10 planes of focus separated by 2 μm were obtained for the same stimulus conditions as the interferograms. The brightfield images were analyzed using Computer Microvision algorithms for comparison with results obtained using stroboscopic interferometry. The noise floor of the system was determined by repeating the same measurements and analysis for images obtained with the stimulus switched off.

In-plane results are shown in Figure 15. For the regions of interest analyzed, a second order resonance was detected at 23 kHz in the x-direction (Figure 15, left panel). The quality factor (Q) was determined to be 40.8 and the noise floor was 0.4 nm. As expected from the design of the device, motions in the y-direction (Figure 15, right panel) are small and comparable to the noise floor (0.6 nm) outside of resonance, the larger amplitude of motion at resonance is due to slight misalignment between the device and camera axes.

Interferometric measurements of out-of-plane motions (Figure 16, left panel) demonstrated a second-order resonant frequency at 28.75 kHz, which was more highly damped with Q=2.75. The noise floor for the measurement was 0.4 nm. Brightfield measurements of out-of-plane motions are similar to the interferometric measurements, but the noise floor is 10 times greater.

The results obtained with the Mirau interferometer are comparable to those for a Linnik interferometer. Both interferometic systems provide much higher out-of-plane resolution than is

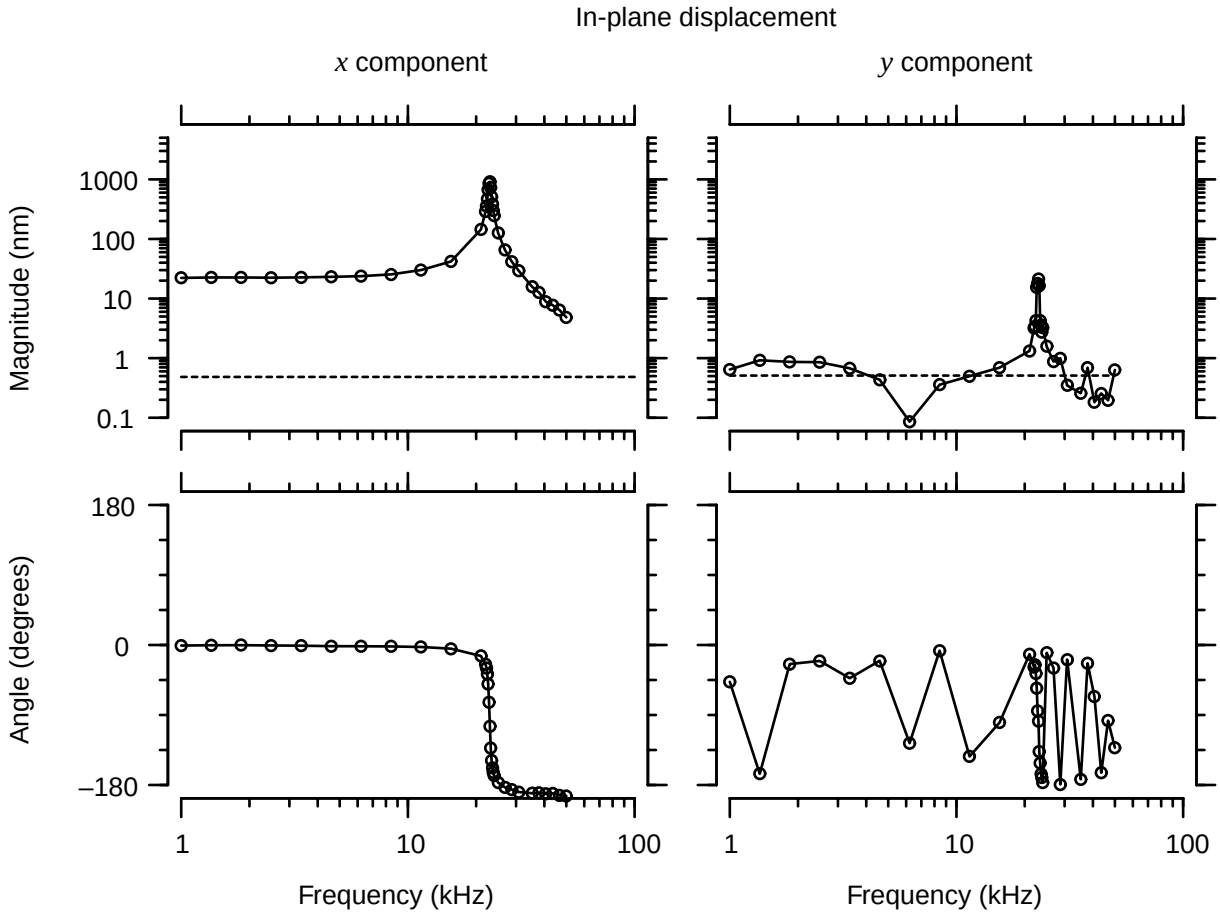

Figure 15: In-plane displacements. The symbols represent the magnitudes (top panels) and angles (bottom panels) of displacements in the intended direction of motion (x, left panels) and in the orthogonal in-plane direction (y, right panels) obtained from analysis of brightfield images. The dashed lines in the top panels show measurements of the noise floor, which is approximately 0.4 nm for the x component and 0.6 nm for the y component.

possible from brightfield image analysis. Out-of-plane resolution from brightfield images depends critically on the out-of-plane resolution of the objective. Thus, high resolution requires optics with high numerical aperture. Out-of-plane motions measured interferometrically do not require high resolution objectives. Generally, high numerical aperture can only be achieved for objectives with high magnifications. The higher the magnification, the smaller the field of view, given the same camera. Thus both interferometric systems provide greater fields of view than a brightfield system with comparable out-of-plane resolution.

The principle disadvantage of the Mirau interferometer is that it greatly reduces the working distance of the optical system. The long-working distance objective that we used has a working distance of 9.8 mm which accomodates for the integration of other pieces of experimental apparatus such as electrical probes or vacuum fixtures. The beam splitter and reference mirror in the Mirau interferometer reduce the working distance to 1.75 mm. This smaller working distance restricts experimental setup in that parts must typically be wire-bonded and the structures to be measured should be near the surface of the package. By contrast, a Linnik interferometer using the same objective would provide the full 9.8 mm of working distance.

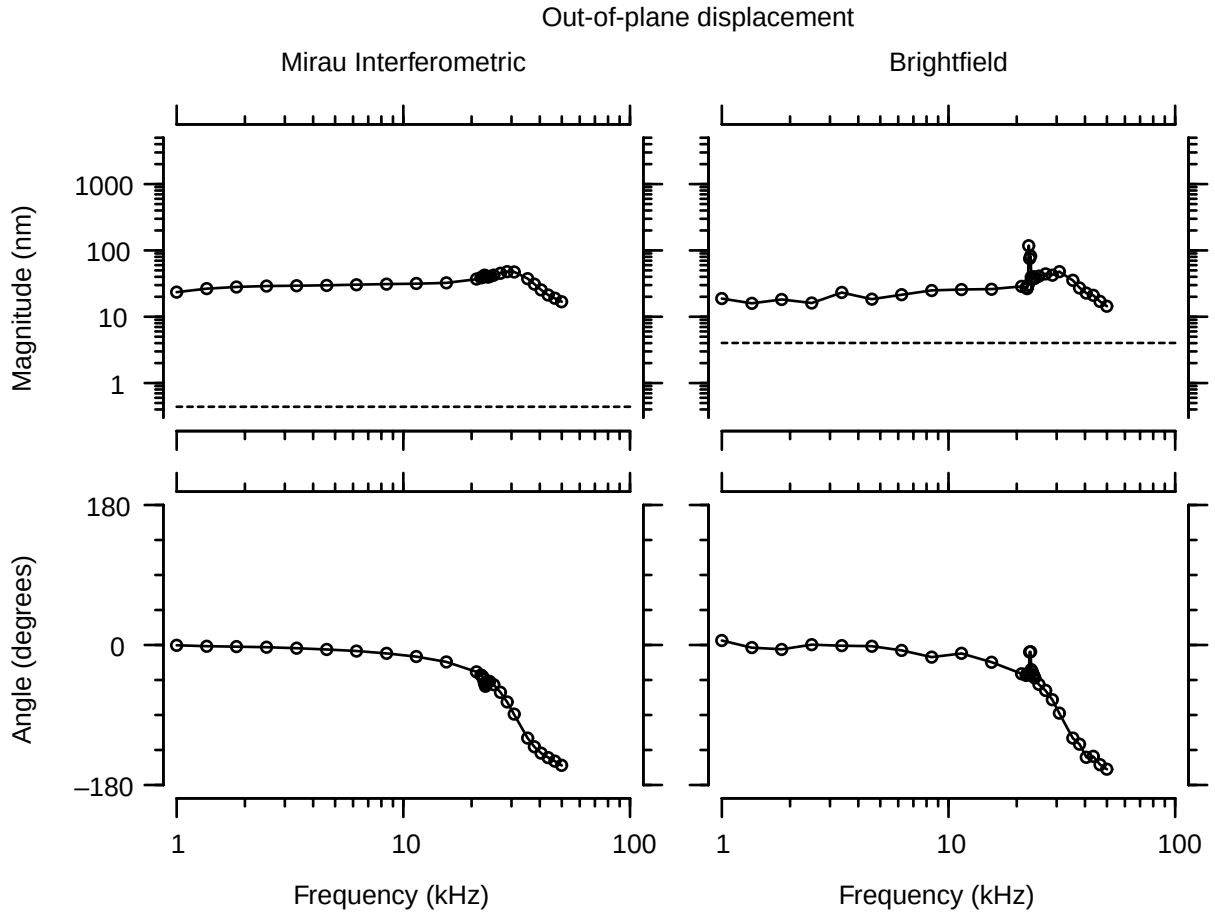

Figure 16: Out-of-plane displacements. The symbols represent the magnitudes (top panels) and angles (bottom panels) of out-of-plane displacements determined by analysis of interferometic images (left panels) and by analysis of brightfield images (right panels). The dashed lines in the top panels show measurements of the noise floor, which is approximately 0.4 nm for the interferometric measurement and 4 nm for the brightfield measurement.

The principle advantage of the Mirau interferometer is that the manufacturer performs the optical alignment. Alignment of the previously designed Linnik interferometer was complicated by the short coherence length of the LED light source (approximately 15 μm). This required the optical path lengths to the target and reference mirror to be matched to within 15 μm. Focusing the target while maintaining the optical paths to this precision was difficult and tedious. By contrast, the Mirau interferometer obviates the need for precision alignment. The results obtained with the Mirau interferometer demonstrate the combination of the superior axial resolution of interference methods with the superior lateral resolution of computer microvision to achieve three-dimensional motions with greater precision and ease.

3.2 Collaborations with MEMS developers

To ensure that the Computer Microvision methods that we develop can be used to address issues that are important to the design and fabrication of MEMS, we have collaborated with MEMS developers to solve problems of practical importance.

3.2.1 Modal analysis of microfabricated gyroscope

We have collaborated with The Charles Stark Draper Laboratory, to investigate motions of their microfabricated gyroscope (Figure 17). The gyroscope is wafer-bonded structure with two proof masses that are driven to move alternately toward and away from each other in a tuning fork fashion. Angular rotations about the axis of symetry between the proof masses induce out-of-plane motions that are sensed by the change in capacitance between the proof masses and conductive plates on the substrate.

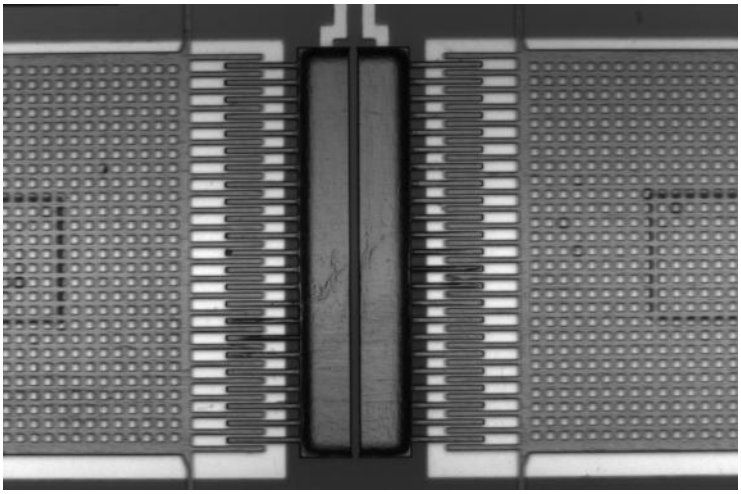

Figure 17: Computer microvision image of a microfabricated gyroscope developed by The Charles Stark Draper Laboratory.

Applying computer microvision to the microfabricated gyroscope provides a number of challenges. First, the lateral (driven) motions of the proof masses are large and the sense (out-of-plane) motions are orders of magnitude smaller. Therefore, this device provides a test of the degree to which motions in one direction confound our ability to measure motions in other directions. Second, the gyroscope is structurally complex and supports many modes of motion. Therefore, this device is an excellent test structure for development of experimental techniques based on computer microvision for modal analysis.

We have applied computer microvision to obtain a modal decomposition of motions of the Draper gyroscope. Two proof masses move alternately toward and away from each other in a tuning fork fashion. Angular rotations about the axis of symmetry between the proof masses induce out-of-plane motions that are sensed as the output. The gyroscope is structurally complex and supports many modes of motion. Motions of the proof masses were measured using computer microvision, and the results were decomposed into components representing both in-plane and out-of-plane modes. Measurements were repeated at different frequencies to characterize the frequency dependence of each mode of motion. In-plane modes were well fit as second order resonances. The

tuning-fork (difference mode) resonant frequency (in air) was 22.8 kHz with quality of tuning (Q) of 202. The hula (common mode) resonant frequency was 20.9 kHz with a Q of 162. Out-of-plane modes were not well fit as second order resonances.

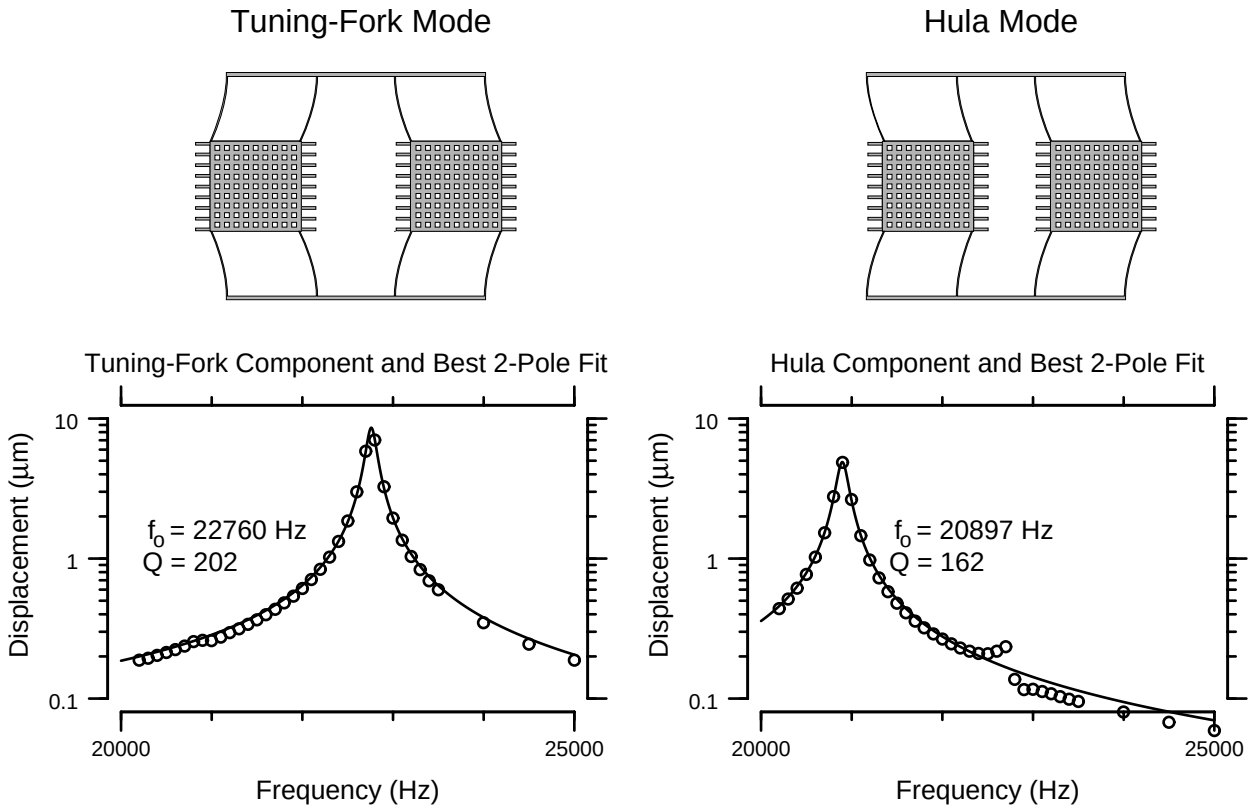

Figure 18: Modes of motion of the Draper gyroscope. In tuning-fork mode (left), the two proof masses move in the same direction. This mode was excited by driving the outer combs of both proof masses with a sinusoidal stimulus. Displacements of each proof mass were measured as a function of time using computer microvision and the results were subtracted to estimate the tuning fork component. The left plot shows the magnitude of this component as a function of the frequency of excitation. In hula mode (right), the two proof masses move in opposite directions. This mode was excited by driving the outer comb of the left proof mass. Displacements of each proof mass were summed to estimate the hula component. The left plot shows the magnitude of this component as a function of the frequency of excitation. The lines are least-squares fits of a two-pole system (left: DC gain is 0.1085 μm, damping coefficient is 0.00247, resonant frequency is 22760 Hz; right: DC gain is 0.077 μm, damping coefficient is 0.03085, and resonant frequency is 20897 Hz).

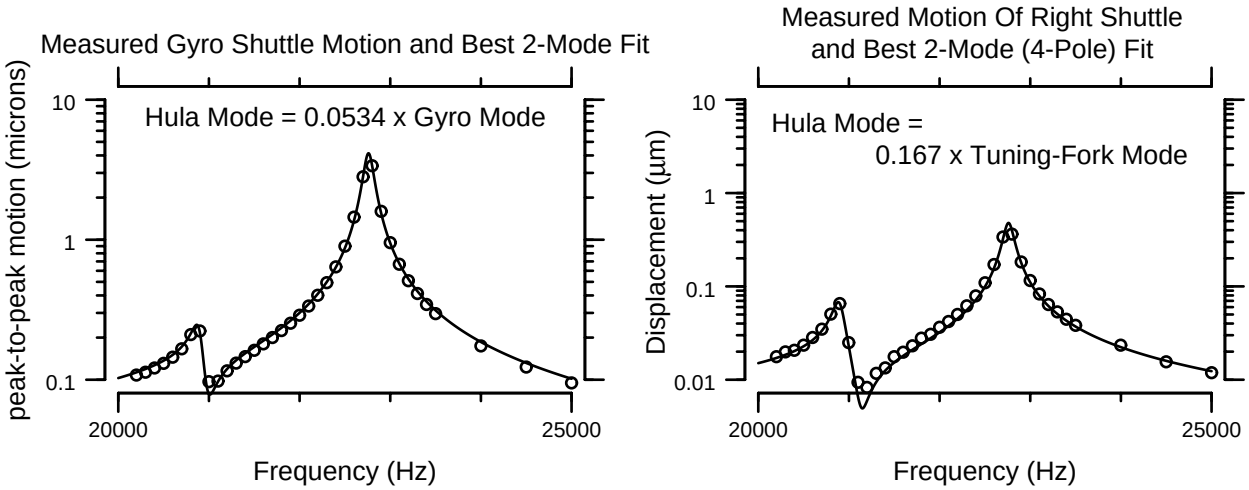

Figure 19: Modal decomposition for other stimulus conditions. The left plot shows the displacement of the left proof mass when the outer combs of both proof masses are driven. The line shows a weighted sum of the modes shown in Figure 18: weights are 0.482 for tuning-fork mode and 0.0363 for hula mode. The right plot shows the displacement of the right proof mass when both combs of the left proof mass are driven with the same voltage. The line shows a weighted sum with weights of 0.0218 for tuning-fork mode and 0.0513 for hula mode.

3.2.2 Calibration of a fatigue test structure

We have collaborated with Exponent Failure Analysis Associates, Inc. to apply computer microvision to measure motions of their reliability test structures (Figure 20, left). The fatigue test structures are being used to investigate effects of stimulus and environmental conditions, as well as manufacturing process conditions, on the performance, aging, and ultimate failure of MEMS [1]. The test structures consist of a proof mass that is rotated about its single point of attachment to the substrate (Figure 20, left panel). Motions are induced by electrical excitation of one comb drive and are sensed by the change in capacitance of the other comb. The goal is to control environmental conditions, to monitor changes in responses, and to formulate quantitative models of reliability for MEMS. Computer microvision was used to calibrate the sensed motion. Figure 20 shows an example.

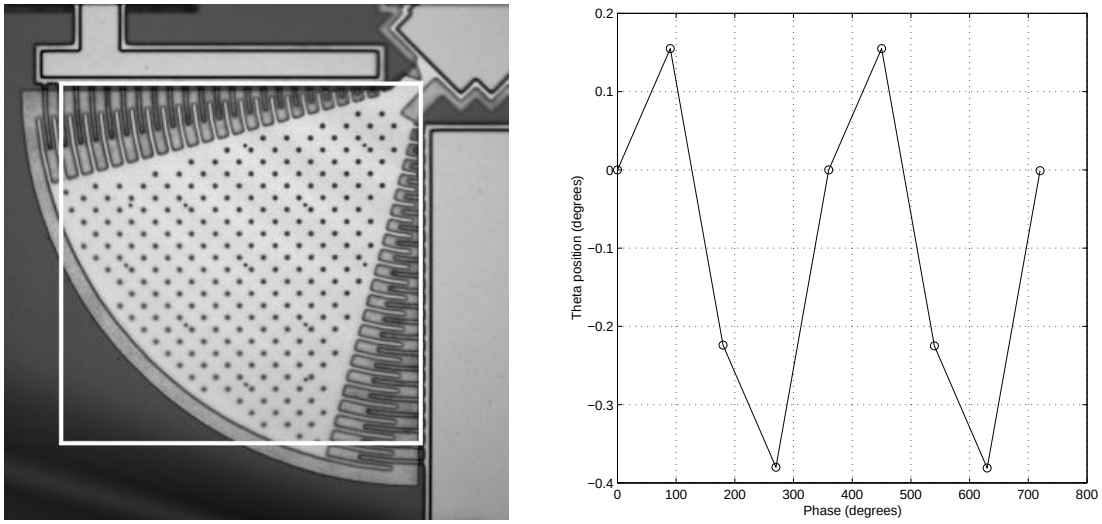

Figure 20: Microfabricated test structure from Exponent Failure Analysis Associates, Inc. A sinusoidal electrical stimulus at 20 kHz stimulated rotations at twice that frequency, and motions inside the region indicated by the white box on the left panel were analyzed. The right panel plots the angular position that was estimated as a function of stimulus phase.

To assess the accuracy of these results, we transformed the image taken at 90° so as to undo the displacements and rotations estimated to have occured between phase 0 and 90°. We then compared this image to the original image at 0°. Results shown in Figure 21 indicate that registration errors are less than 0.1°.

Meaningful interpretations of results of fatigue tests require accurate measurements of the motions that lead to fatigue. We have applied computer microvision obtain such calibrations Figure 22. The standard deviation for repeated trials is less than 0.002 degrees at all amplitudes.

Because it is simple, the fatigue test structure is also useful for developing experimental techniques for 3D motion analysis. The proof mass is attached at a single point. The resulting modes of motion are simple torsion modes. By contrast, motions of more complex structures (such as those of the Draper gyroscope, previous section) cause not just torsion but also tension in the support beams. The tension is a nonlinear function of the displacement of the proof masses.

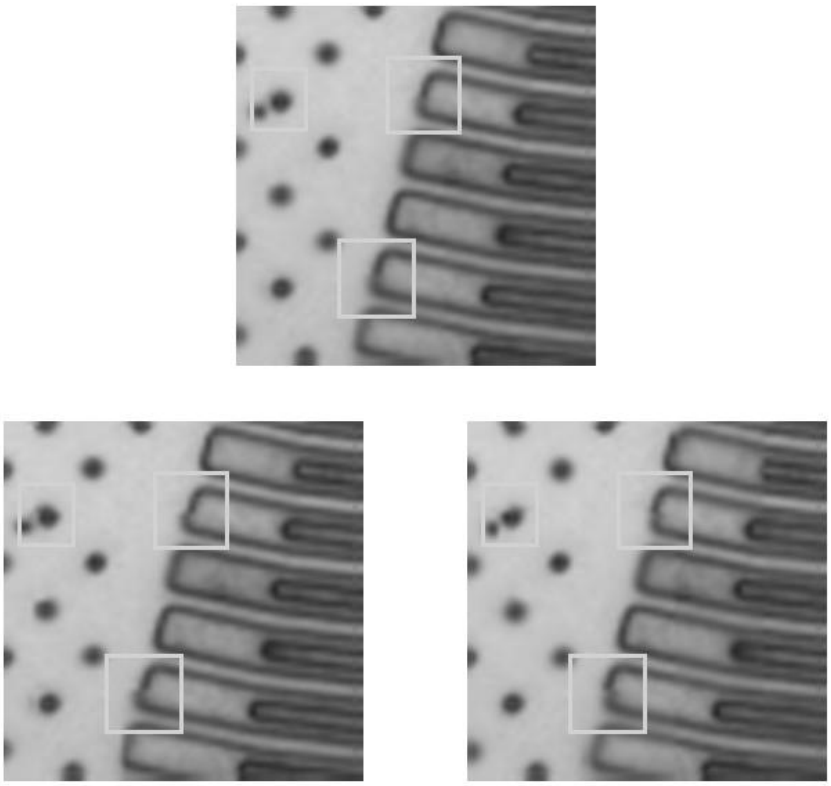

Figure 21: Accuracy of rotation estimates. The image at $90°$ was transformed so as to undo the displacements and rotations estimated to have occured between phase 0 and $90°$. Portions of the resulting image where then interleaved (using a checkerboard pattern) with the original image taken at $0°$ (upper panel). If the estimate were perfect, the pieces should fit together with no misalignment. The bottom panels show results when the image at $90°$ was rotated by $0.1°$ more than was estimated and by $0.1°$ less. Worst case misalignment (indicated by the white squares) is greater in the lower panels than in the upper panel, showing that errors in our estimates are less than $0.1°$.

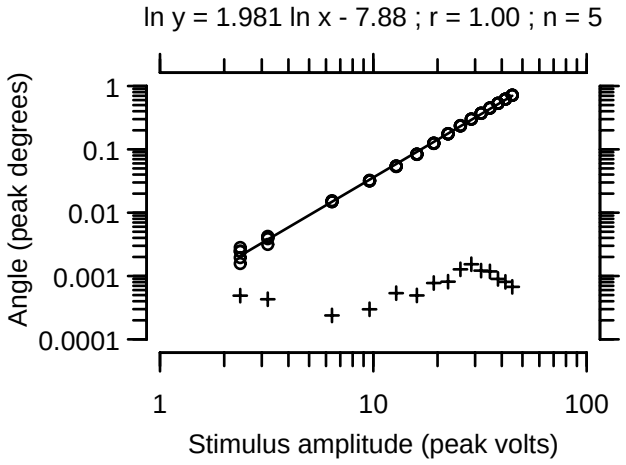

Figure 22: Calibration of a fatigue test structure. The fatigue test structure developed by Exponent Failure Analysis Associates, Inc. was stimulated at resonance with a sinusoidal voltage. Five independent measurements (circles) were made at each of 15 different amplitudes (abscissa) of stimulation. The line, which is given by the equation at the top of the plot, is a regression line fit by a least squares method. The plus symbols (+) indicate the standard deviations of results at each amplitude.

Thus, motions of complex structures are nonlinear. Nonlinearities of Exponent Failure Analysis Associates' fatigue test structure are orders of magnitude smaller. Linearity simplifies both measurement and finite-element analysis of modes of motion of this device. Figure 23 illustrates three-dimensional motions of the fatigue test structure obtained using computer microvision. Angular displacements were computed from measurements of three-dimensional translations at multiple points on the proof mass. Results were obtained as a function of stimulus frequency to determine the best frequencies and quality of tuning for dominant modes of motion. Results show high quality resonance for angular displacements in the plane of the proof mass and low-pass behaviors for out-of-plane levitation and rocking.

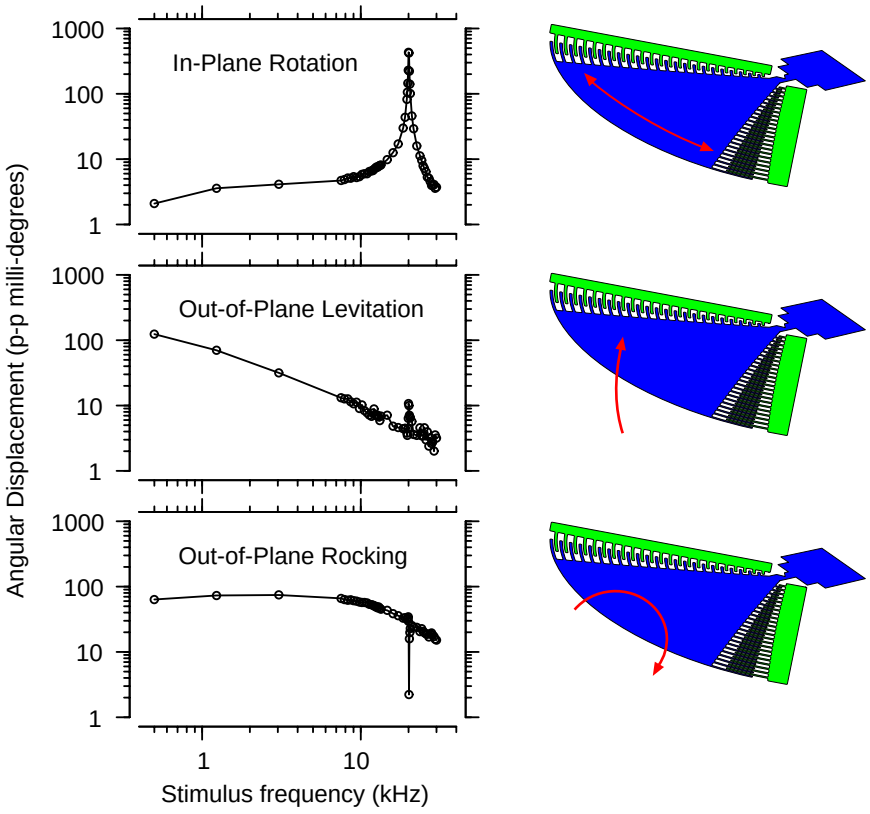

Figure 23: Three-dimensional rotations of fatigue test structure. Motions were excited with constant amplitude (60 V p-p) stimuli at 56 frequencies. Mechanical responses are at twice the stimulus frequency. Images at 12 focal planes (2 μm spacing) were analyzed to determine in-plane rotation, out-of-plane levitation, and out-of-plane rocking. Results are displayed as angular displacements. The outlier point in the out-of-plane rocking measurements falls exactly on the in-plane resonance frequency.

3.2.3 Resonance analysis of 3D motion sensors

Figure 24 shows a gyroscope developed by Wyatt Owen Davis, working with Professor Albert P. Pisano at the Berkeley Sensors and Actuators Center. Behavior in linear and nonlinear regimes has been identified and quantitatively analyzed (Figure 25 and Figure 26).

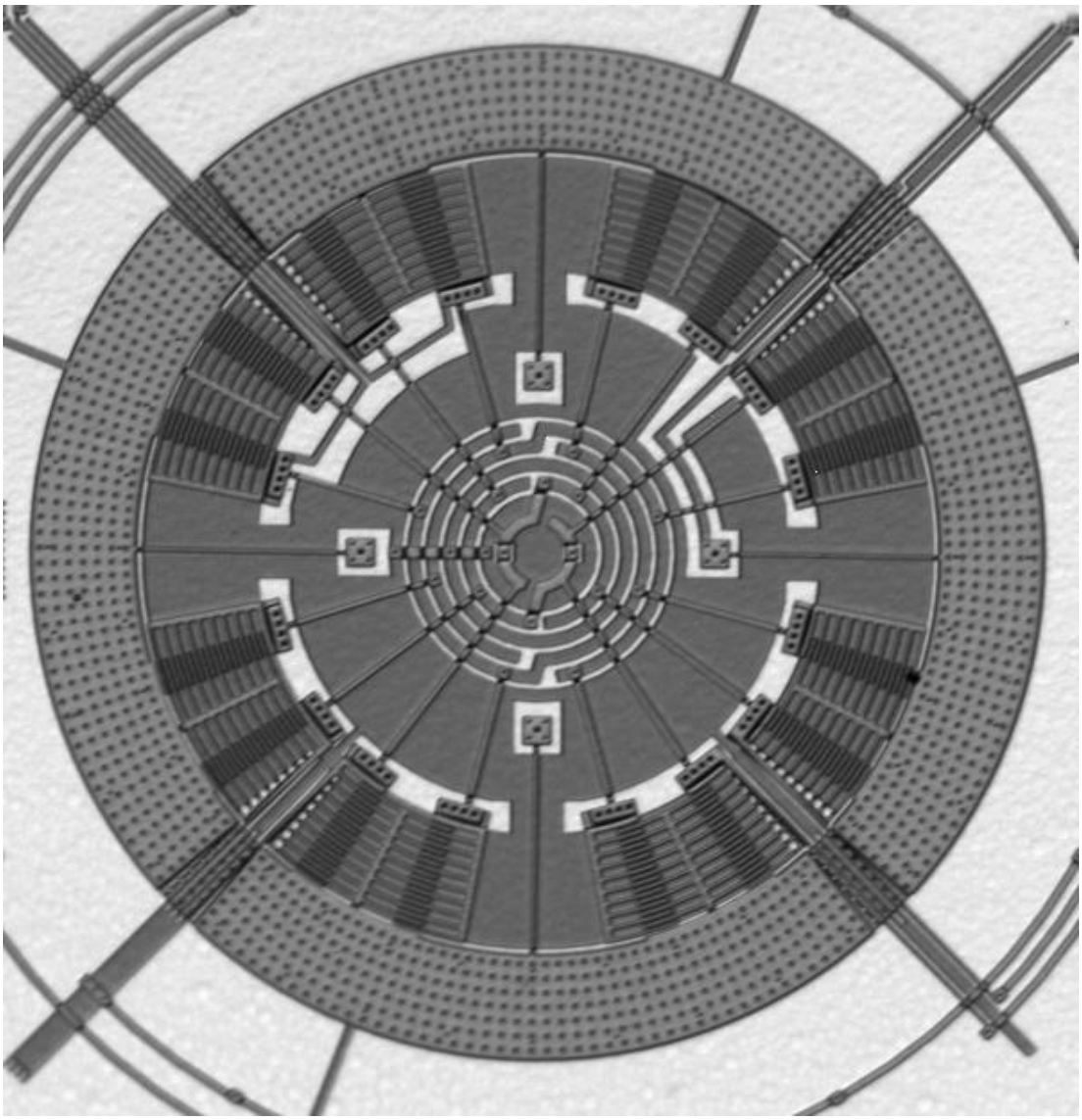

Figure 24: Gyroscope developed by Wyatt Owen Davis at the Berkeley Sensors and Actuators Center. The inner radius of the moving ring is 200 microns. The outside radius is 250 microns. The diameter of the whole device is 500 microns. (Christian Rembe, BSAC)

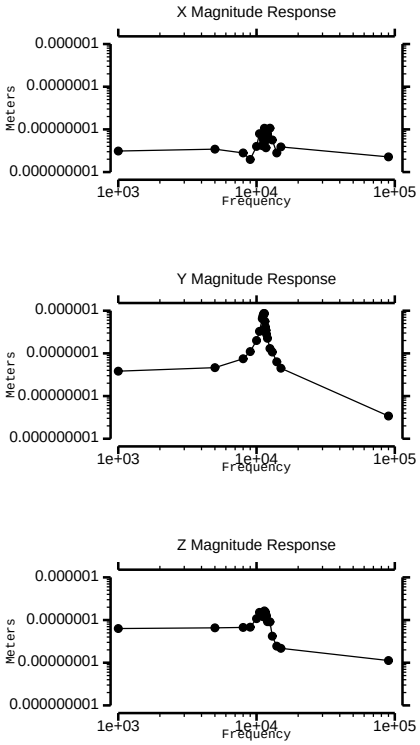

Figure 25: Displacement amplitude frequency response of BSAC gyroscope with a sinusoidal stimulus of 10 Volts DC plus 5 volts AC

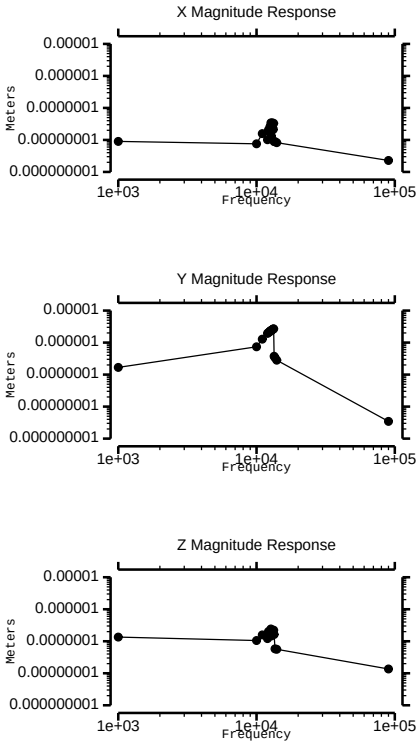

Figure 26: Displacement amplitude frequency response of BSAC gyroscope with a sinusoidal stimulus of 20 Volts DC plus 10 volts AC

3.2.4 Characterization of CMOS MEMS

The Computer Microvision system at Carnegie-Mellon University (CMU) has now been used extensively in 5 research projects. We illustrate one example: measurements of a MEMS gyroscope device designed by Hao Luo in Professor Gary Fedder's laboratory. The measurements were made by Huikai Xie.

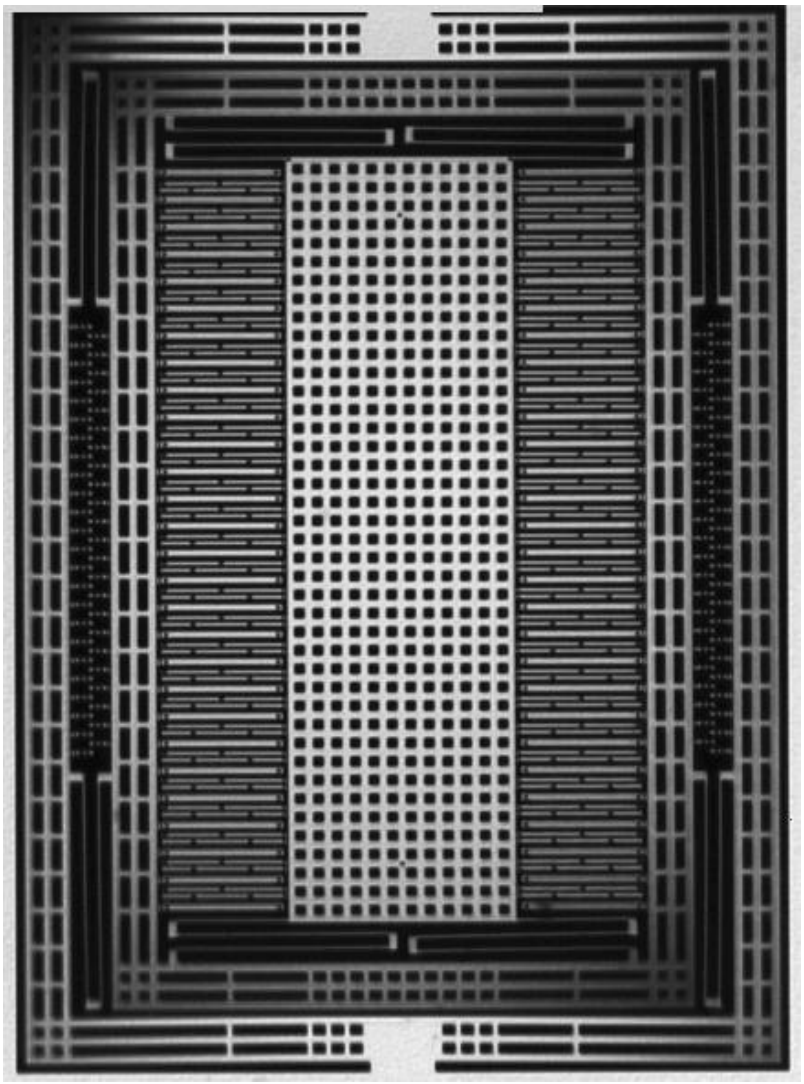

Figure 27: CMU MEMS gyroscope device.

Figure 27 shows a photograph of the gyroscope taken using the Computer Microvision system. The gyroscope was fabricated using CMU's CMOS MEMS fabrication technique, which integrates MEMS with CMOS electronic devices. The device is anchored near the top center and bottom center of the photo. The outer square frame holds the fixed stator fingers (the short stubby fingers) in the far left and right of the photo for driving the nested accelerometer in the x direction. The inner square frame has long fingers on its inside edge that sense y-motion of the central perforated proof mass in a differential parallel-plate mode. Therefore, the x direction is drive, the y direction is Coriolis sense. The frequency response of the gyroscope as measured by analysis of data from

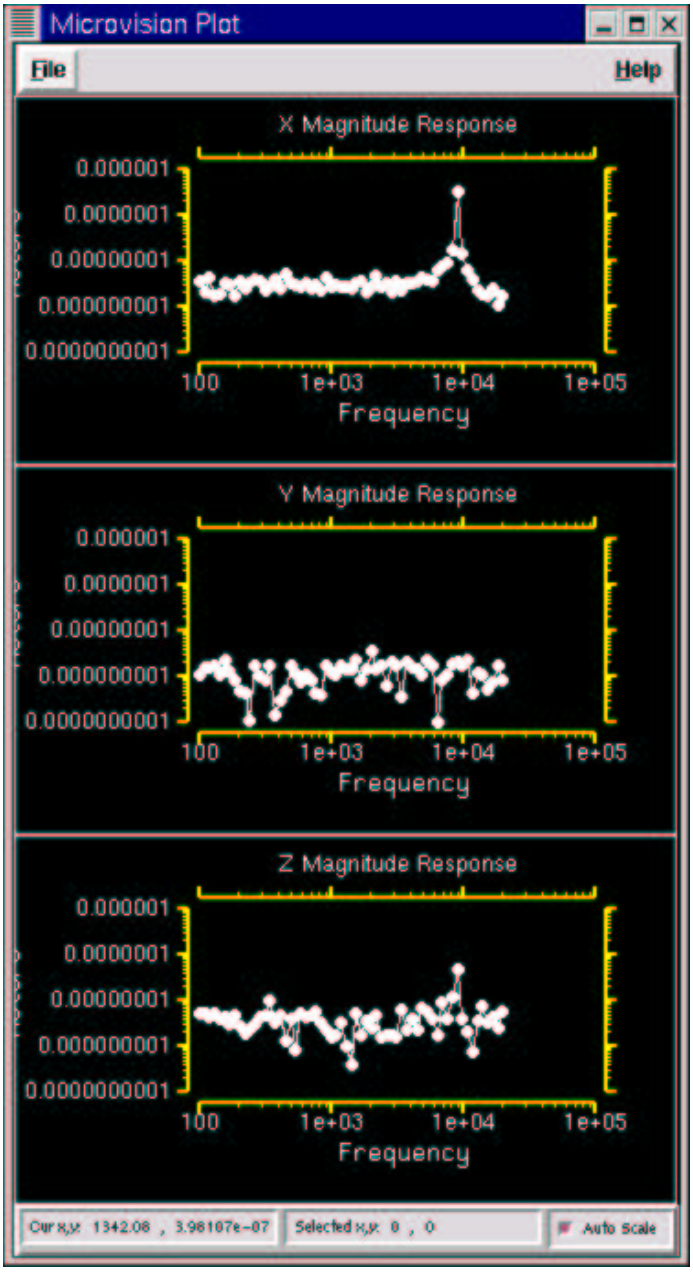

Figure 28: Frequency response of MEMS gyroscope. Test conditions were a sinusoidal stimulus of 2 volts amplitude with a DC offset of 18 volts.

the Computer Microvision system is show in Figure 28.

3.2.5 Displacements of optical gratings

In collaboration with James Castracane at the University of Albany, we have applied Interferometric Computer Microvision to measure MEMS optical gratings (Figure 29). The gratings consist of an array of slender elements, each approximately 12 μm wide. Our goal was to measure the out-of-plane positions of the elements.

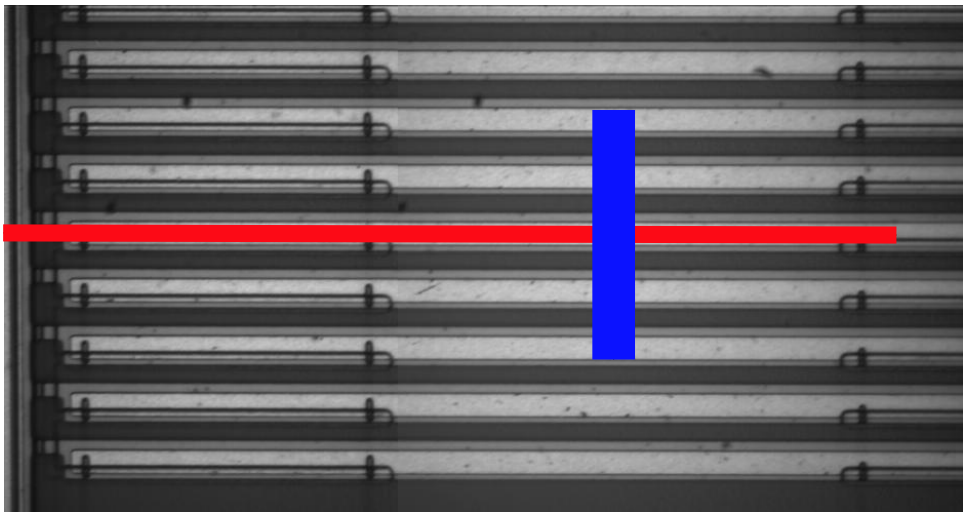

Figure 29: MEMS optical grating. This brightfield image shows a portion of the optical grating that contains 8 horizontal elements, each of which is brighter than the surrounding substrate. The elements are more than 300 μm long and their centers are 20 μm apart. Voltages can be applied between the elements and the substrate to modulate the out-of-plane distance and tilt of the element. The red and blue bars mark analysis regions. The length of the red bar is 300 μm.

Interferograms were obtained for 3 positions of the reference mirror for each of 7 excitation voltages (DC). Brightnesses in the 3 interferograms were used to determine the optical phase of the interference at each pixel. Phases were "unwrapped" by adding the integral multiple of 2π that minimized first spatial differences.

Results shown in the left panel of Figure 30 illustrate bending of the elements as a function of distance along the long axis of the element. In the absence of DC excitation, the element sags approximately 1 μm across its more than 300 μm length. The bending increases as the applied voltage is increased. Measurements of the adjacent substrate show no similar sagging.

The right panel of Figure 30 shows out-of-plane displacement across 5 adjacent elements. Displacements were obtained for the more than 25 pixels that span the approximately 12 μm width of each element. Although these elements are designed to tilt, little tilt is seen in these measurements.

These results clearly indicate that Interferometric Computer Microvision can be used to assess both out-of-plane position and tilt of MEMS optical gratings.

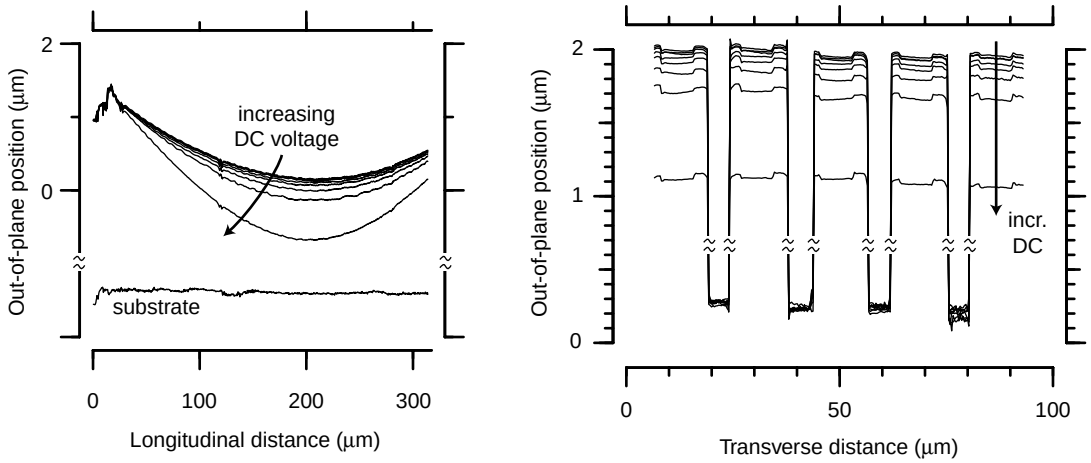

Figure 30: Out-of-plane positions of grating elements. Curves in the left panel indicate out-of-plane position (ordinate) as a function of distance along the length of a grating element (red line in Figure 29). Each of the upper curves shows results for a different excitation voltage from 0 to 30V in 5V steps. The lower trace shows the out-of-plane position of the substrate lateral to the measured grating element. No attempt was made to determine the number of phase wraps between the element and substrate, as indicated by the broken axis. Curves in the right panel indicate out-of-plane position across the widths of 5 elements (blue line in Figure 29) for the same excitation voltages.

3.2.6 Alignment of optical switches

We have applied computer microvision to measure optical alignment of microfabricated mirrors developed by Ming Wu and the University of California in Los Angeles (UCLA). The mirrors are oriented so that their reflecting surface is nearly perpendicular to the substrate. Our goal was to apply video microscopy to determine the angle between the mirror surface and substrate with subdegree precision.

To determine the orientation of the mirror, we measured the three-dimensional positions of multiple points on its surface, including points along the perimeter of the mirror as well as points on the edges of release holes. The best fitting plane through measurements of 6 to 12 points was determined using a least squares technique. The equation for the plane was used to derive the direction cosines for the vector normal to the plane.

The reference frame for the normal vector is that of the video microscopy system. To relate the orientation of the mirror to that of the substrate, we could have simply repeated the procedure to determine the orientation of the substrate. Alternatively, we can take advantage of the fact that the substrate also acts as a mirror, and we can see a reflection of the mirror in the substrate (Figure 31).

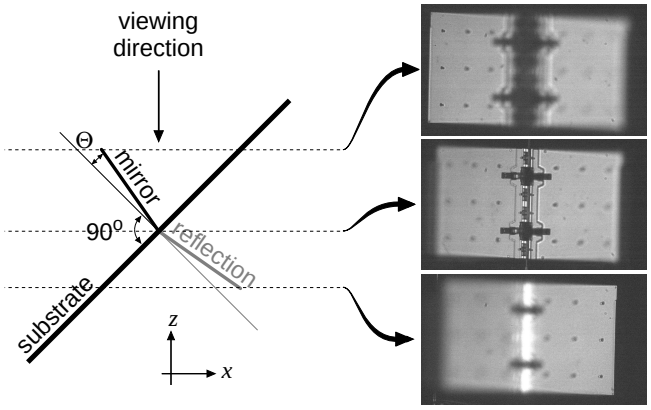

Figure 31: Three-dimensional image of the microfabricated mirror and its reflection in the substrate. For measurement purposes, the chip was mounted with the substrate at an angle of approximately 45° relative to the viewing direction (left panel). In this orientation, the top and bottom edges of the mirror were in best focus at two different planes of focus (top two images). At a deeper plane of focus (bottom), the reflected image of the mirror could be seen.

The principle advantage of measuring the orientation of the reflection is that the optical alignment problem can then be cast into a registration framework. Consider a cube of image data that contains the reflection of the mirror. If the data in that cube are first reflected about the z axis (see Figure 31) and then about the x axis, the reflection will then be oriented nearly the same as the mirror. If the mirror is exactly orthogonal to the substrate, then the mirror and reflection will be parallel. If the mirror is tilted an angle Θ off the perpendicular, then the reflection will be rotated by 2Θ relative to the mirror. Thus the alignment angle Θ can be determined by registering the mirror with its reflection.

Image resolution is limited by the optics [6]. To a first approximation, images are blurred by convolution with a point-spread function [4] with dimensions on the order of the wavelength of light (525 nm for our system). Therefore, the precision with which absolute positions of targets can be determined is on the order of micrometers. However, one can align blurred images to significantly greater precision. Registration errors as small as nanometers can be reliably measured [3].

We have obtained 3D images of the mirror and reflection, and we have determined mirror alignment by manually identifying fiducial points on the mirror and reflection. Variability between repeated trials suggests that these methods result in subdegree precision.

3.2.7 Modal analysis of LIGA fail-safe device

In collaboration with the Naval Surface Warfare Center, Indian Head Division, we conducted tests to assess the use of Computer Microvision to perform dynamic mechanical tests of LIGA MEMS.

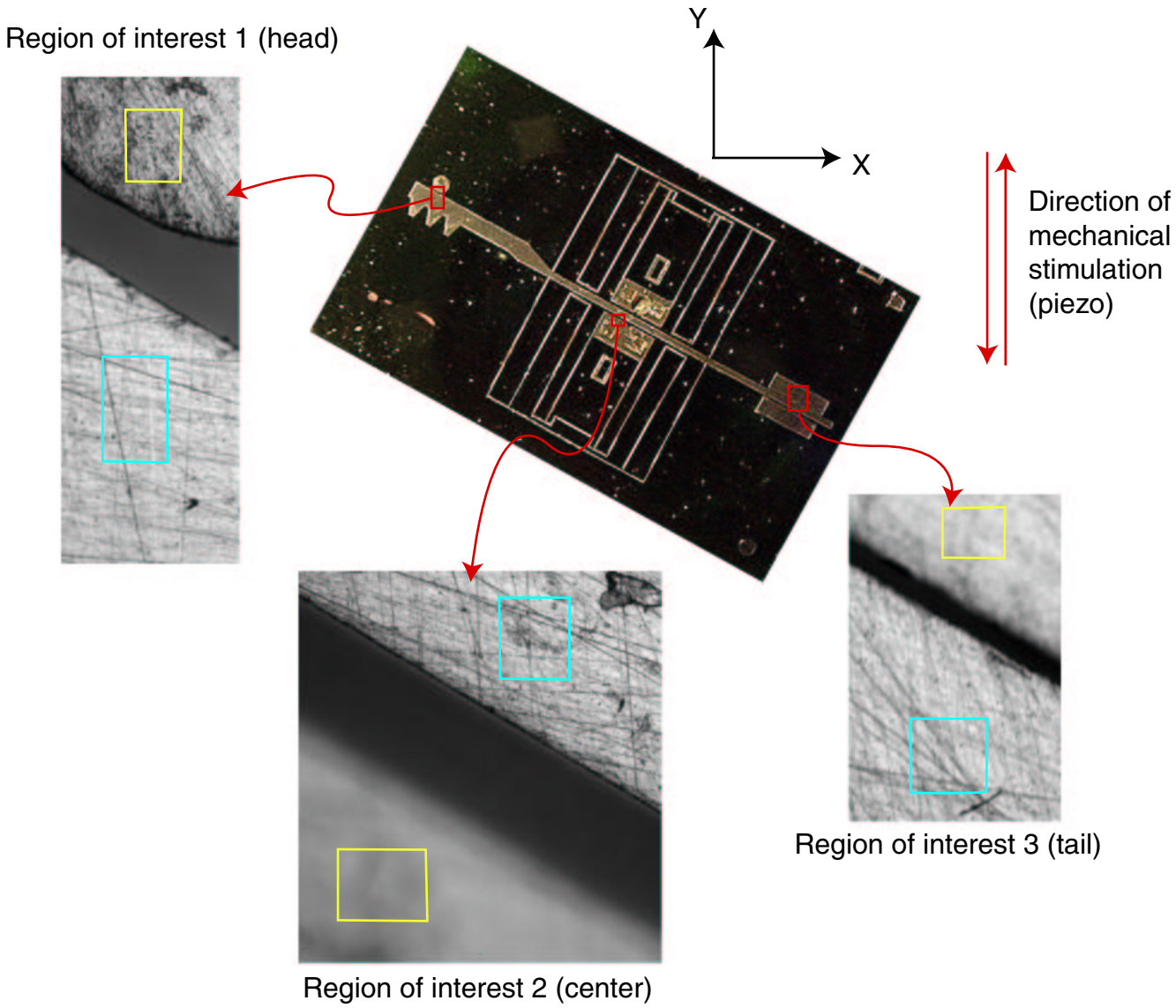

Figure 32: Orientation and analysis of motions of "Device B." The tilted photograph shows the orientation of Device B relative to the mechanical stimulus: the angle between the long axis of the shuttle and the direction of mechanical stimulation (vertical) is approximately $65°$. The red boxes indicate regions of the device whose motions were analyzed. Magnified views of each analysis region show analysis regions on the shuttle (blue boxes) and on structures attached to the substrate (yellow boxes). Each region includes part of the shuttle. Analysis regions for the shuttle are outlined in yellow. Analysis regions for the substrate are outlined in blue. Motions were analyzed in the X and Y directions indicated by the arrows.

The test structure, Device B, consists of a slender "shuttle" that is attached via folded springs to the substrate. The device was mounted to a platform attached to a piezoelectric crystal, so that the device could be moved parallel to its plane. The device could be rotated in its plane to change

the direction of the applied motion. We summarize results obtained for the orientation shown in Figure 32, in which the angle between the long axis of the shuttle and the direction of mechanical stimulation was approximately $65°$. This orientation was chosen in an attempt to stimulate modes other than the main mode in which the shuttle travels parallel to its long dimension.

3.2.7.1 Substrate motions

To characterize substrate vibrations induced by the piezoelectric crystal, we measured motions of the substrate at 3 different points (Figure 32). Results for 41 frequencies ranging from 100 Hz to 20 kHz are shown in Figure 33. Motions in the intended direction ranged from 0.6 to 1.44 μm for frequencies up to 10 kHz. Motions in the unintended direction were everywhere less than 0.3 μm.

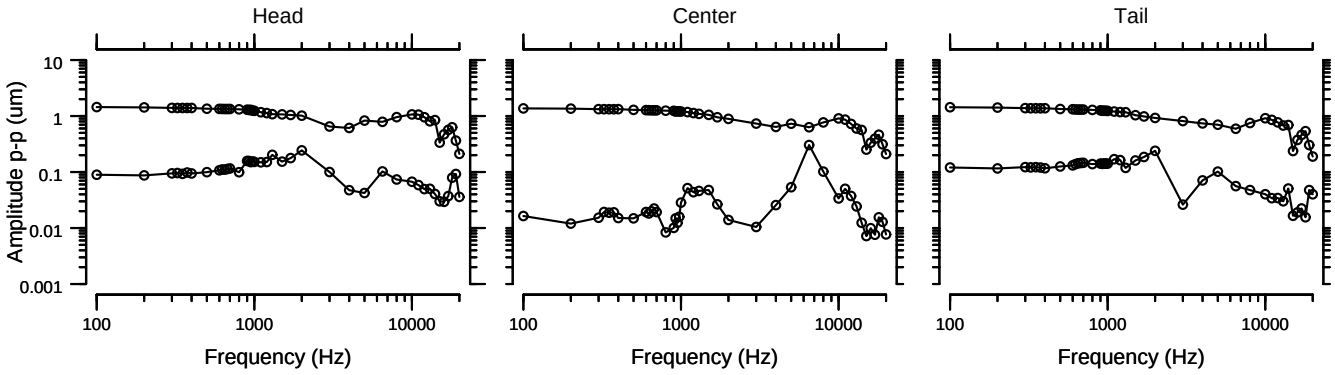

Figure 33: Driven substrate motions. Motions of the substrate were driven by applying fixed-amplitude sinusoidal voltages to the piezoelectric crystal. Each panel shows the frequency dependence of peak-to-peak displacements of a portion of a structure attached directly to the substrate. The left, center, and right panels show results for regions near the head, center, and tail of the shuttle, which are shown in Figure 32. In each panel, the top curve connects components of displacement in the intended (Y) direction of excitation, and the bottom curve connects components in the unintended (X) direction. Notice that the displacement scale is logarithmic, and spans 4 orders of magnitude.

3.2.7.2 Shuttle motions

Motions of the substrate induced motions of the shuttle, and measurements are shown in Figure 34. Motions of the shuttle were primarily in the Y direction. In contrast, the X and Y components of motions of the shuttle were comparable in magnitude.

X displacements at 300 Hz were prominent at all three measurement sites. Examination of the video images showed that these large motions at 300 Hz were primarily directed along the long axis of the shuttle, suggesting that 300 Hz is an important longitudinal resonance frequency. X displacements at 950 Hz are prominent in the center and tail regions of the shuttle, suggesting a second mode of motion near 950 Hz.

Y displacements at 650 Hz are very prominent in the tail region, and visible in the center. Differences in the displacement at 650 Hz at different regions suggests that this frequency could correspond to a rotational mode.

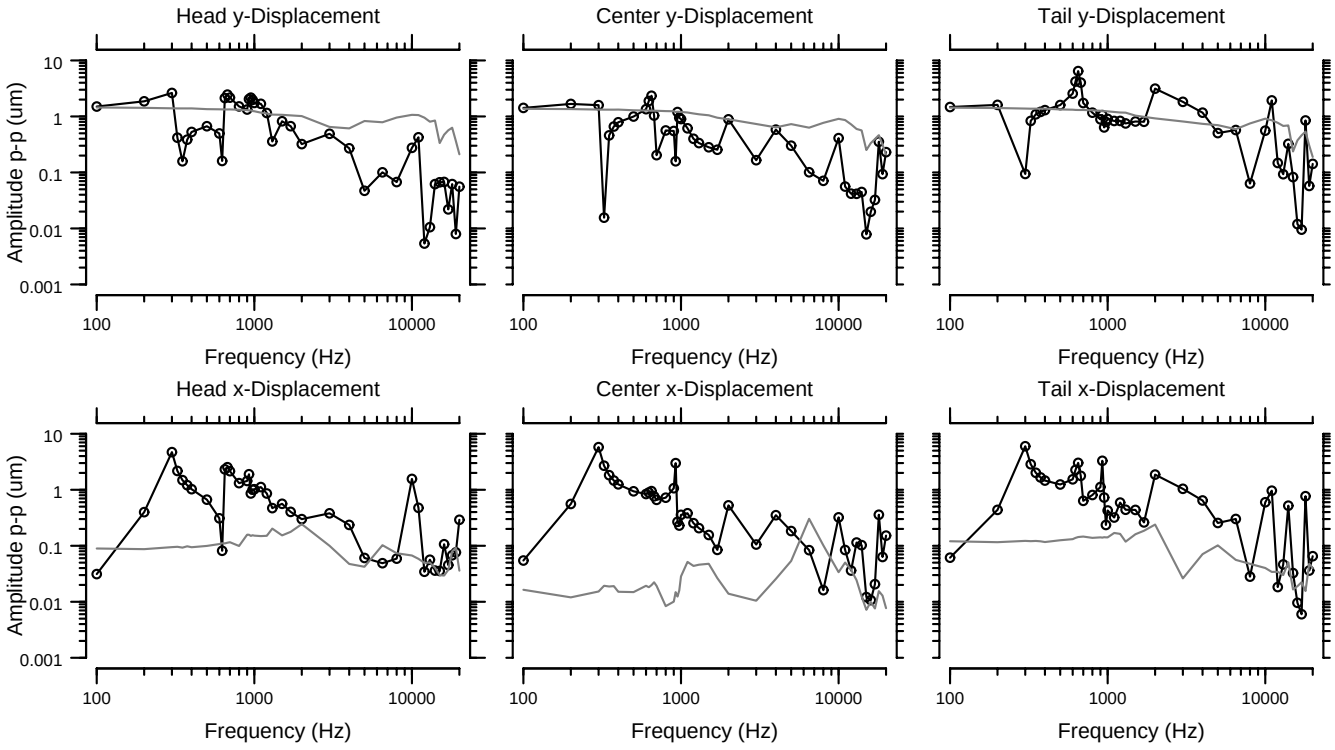

Figure 34: Shuttle motions. Motions of the shuttle were measured from the same images used to determine substrate vibration (Figure 33). The top panels show the Y components of motion, and the bottom panels show the X components. The corresponding substrate displacement from Figure 33 is shown by the gray line. Other aspects of this figure are as described in Figure 33.

3.2.7.3 Detailed analysis of motion at 650Hz

Figure 35 shows a closer look at the complex mode of motion at 650 Hz. Displacements near the head and tail are nearly in phase opposition, and the magnitudes of the displacements near the center are smaller than those at the ends. These data support the notion that the mode of motion at 650 Hz is rotational.

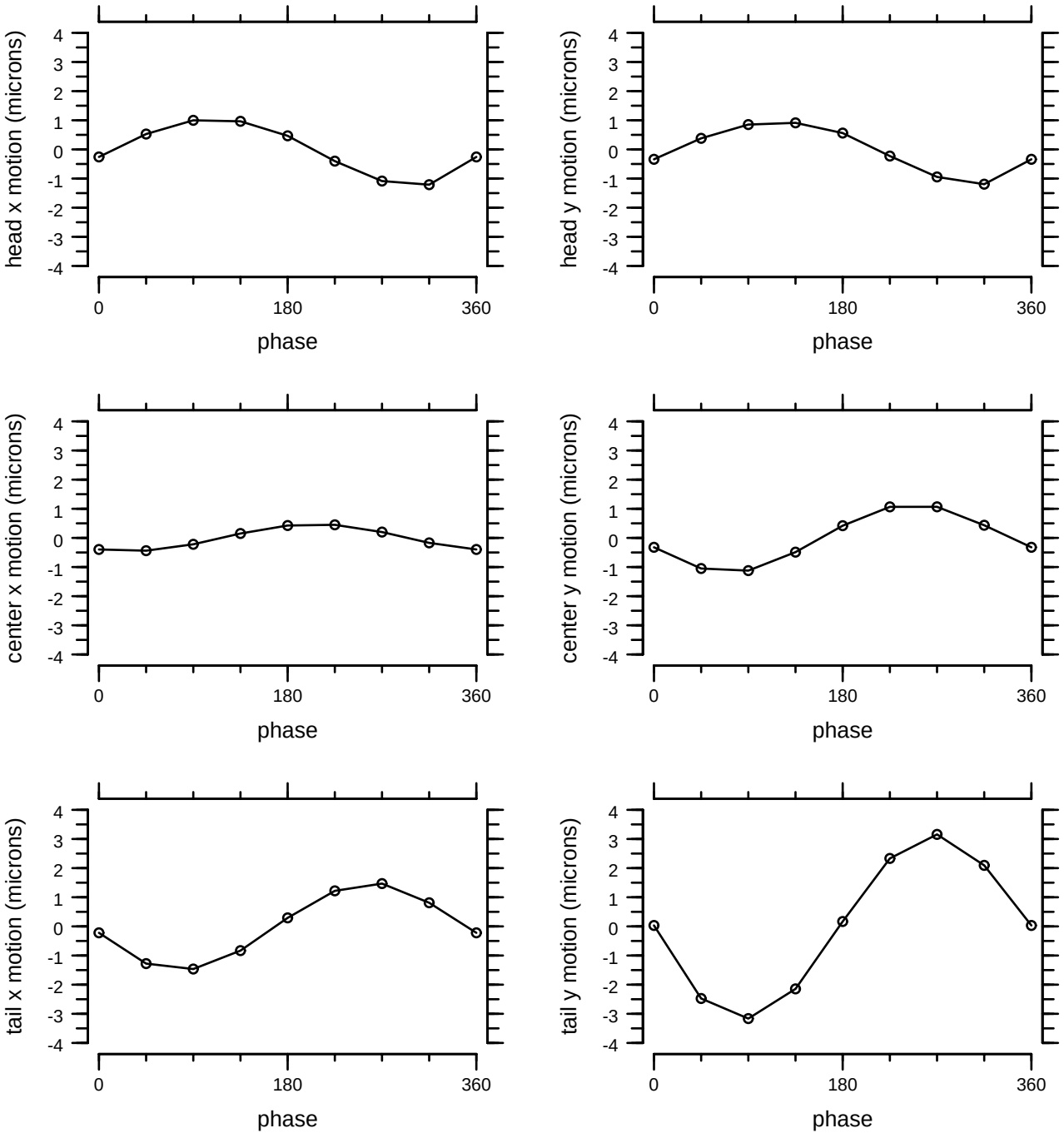

Figure 35: Measured motion amplitudes of the shuttle at 650Hz. The top row contains plots of the motion of the head. The middle row contains plots of the motion of the center. The bottom row contains plots of the motion of the tail. In each row x motions are plotted on the left and y motions are plotted on the right.

In summary, we stimulated motions of Device B by attaching the device to a piezoelectric crystal and vibrating the substrate. Direct measurements of the resulting substrate vibrations showed good control of the stimulus for frequencies from 100 Hz to 10 kHz. Direct measurements of the shuttle revealed a number of resonant modes, where motions were larger than those of the substrate. A primary mode at 300 Hz generated large motions parallel to the long axis of the shuttle. A second, rotational mode was seen near 650 Hz. We conclude that Computer Microvision is a sensitive tool for performing dynamic tests of LIGA MEMS.

3.3 Multi-beam interferometric optical imaging for MEMS

We have developed a novel form of microscopy based on the interference of multiple coherent beams. In a typical light microscope, the light source is optically crude, providing approximately uniform illumination to the target. On the other hand, the microscope objective, the first and most critical element in the imaging chain, is optically sophisticated. Therefore, the optical quality of the objective is primarily responsible for the optical quality of the microscope. In the multi-beam interferometric approach we adopt an alternative strategy: coupling highly precise structured illumination from a laser source with a relatively crude detection system. Using laser light with beam-splitting and steering techniques, we can generate precisely structured illumination, such as high-spatial-frequency fringe and speckle patterns. These patterns selectively excite microscopic features of the target. Therefore, the key to resolution in the revised strategy is in the illuminator — not in the detector. By using finely-patterned laser illumination, we can obtain high resolution images using low resolution optics and a CCD camera.

Pixels in a CCD camera report a single output value that represents the sum of the photons that strike any part of the pixel. By controlling the fine structure of the source of illumination, low resolution pixels become sensitive to high resolution structure in the target. After acquiring a sequence of images with different structured illumination patterns, we can use a computer to post process the images and enhance the resolution of each CCD pixel to the resolution of the illumination patterns.

3.3.1 Experimental verification of theory. We have constructed a series of prototypes, each designed to test practical engineering ideas as well as fundamental science. The experimental verification of multi-beam inteterference theory marked the completion of a Ph.D. thesis: *Synthetic Aperture Microscopy*, by Michael Mermelstein, a Hertz Fellow and member of our research group. The thesis reports on the theory of multi-beam interferometric microscopes, on engineering practical ones, and on the group's progress with various prototype experimental systems.

One of our prototypes, shown in Figure 36, uses forty-one (41) beams from an argon ion laser operated at 488 nm (blue) to generate finely-structured illumination. The phase of each beam is controlled by a custom 128 channel digital-to-analog converter under computer control. Light reflected from the target is collected by a 256×256 pixel CCD camera with 16 μm pixels and a 2× copy lens.

The Fourier transform of a measured illumination pattern created by the interference of these 41 beams is shown in Figure 37. This measurement contains a pattern of 1,641 bright spots (two for each beam-pair and one at the origin) located in accordance with the theoretically predicted arrangement. The figure demonstrates the prediction that the patterns created by the 41 beams provides an excellent and predictable sampling of Fourier space.

The outer ring of points in the Fourier transform marks the highest spatial frequency that is sampled, which corresponds to a resolution of 0.2 μm (with 0.488 μm illumination!). This corresponds to a factor of 40 increase in the effective resolution of the CCD and lens system. Furthermore, this high resolution is achieved with large working distance (greater than 12 cm) and field of view (greater than 4 mm square).

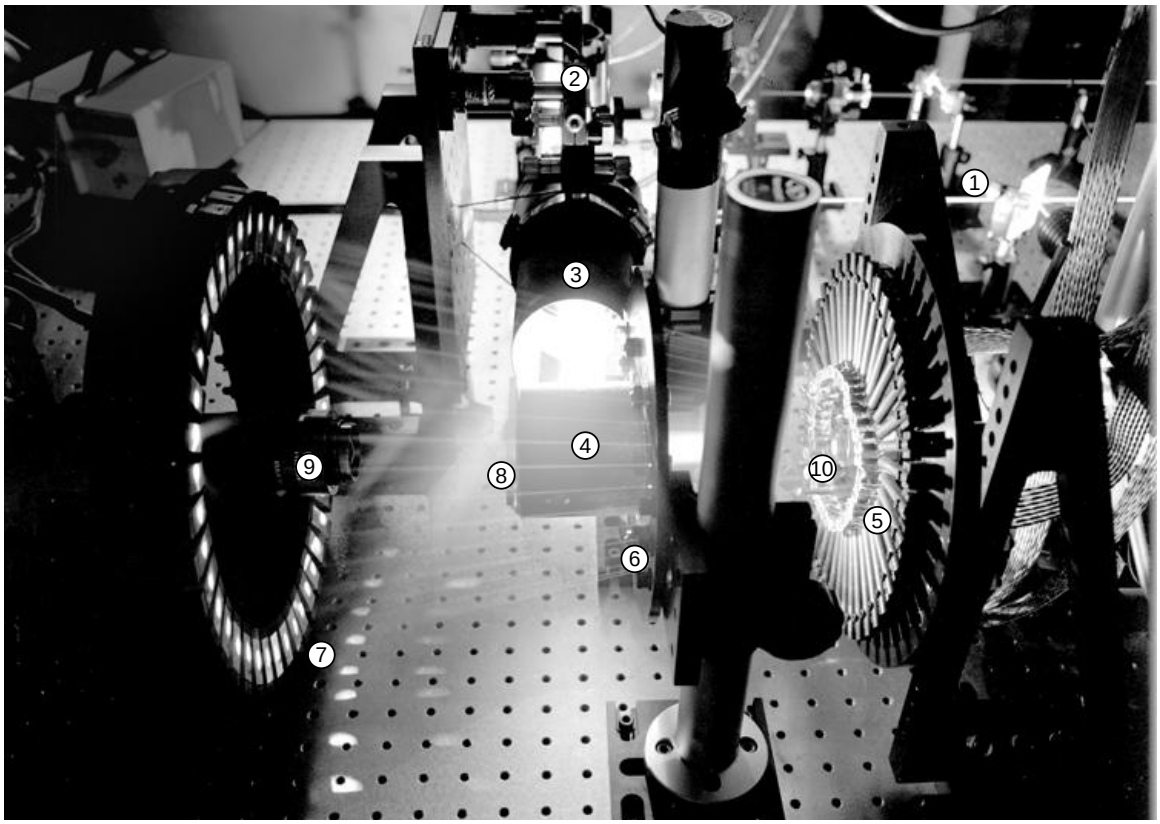

Figure 36: A multi-beam interferometric microscope experimental setup. The labels indicate (1) the source beam from the argon ion laser (laser head not shown) which passes through a spatial filter before entering (2) a periscope assembly which directs the expanding beam into (3) a large aperture copy lens. The now converging beam enters (4) the hologram housing which contains an elliptical fold mirror and the beam-splitting hologram. A diverging cone of 41 converging beams emerges from the right side. The beams strike (5) the ring of path-length modulating mirrors, one beam per mirror. Each mirror is glued to a piezo which is glued to a steel drill-rod post. Each post is fastened to a miniature tip-tilt mount to facilitate alignment with (6) the "slit array," an array of matched spatial filters at the unfolded focus point of the copy lens. The now diverging beams strike gratings in (7) the grating wheel from which they diffract. Second-order diffracted beams are the strongest (because of the blaze angle of the gratings), and a converging cone of diverging second-order beams land on (8) the target where they interfere, **forming the finely-structured illumination pattern.** Light scattered or fluoresced by the **illuminated micro-regions** of the target is collected by (9) the target **camera macro lens.** First-order diffracted beams from the grating wheel pass through angled cuts in the slit-wheel mounting plate and interfere in the focal plane of (10) the reference camera microscope objective lens for calibration of the phase offsets of the many beams.

3.3.2 Summary. Multi-beam Interferometric Microscopy enables

- Order-of-magnitude **improvement in depth of field.** This improvement is particularly useful for high-resolution inspection of MEMS systems with substantial depth compared to in-plane detail such as (1) hinged, tilted devices like 90-degree mirrors, (2) high aspect-ratio MEMS, and (3) MEMS interface to packaging feed-throughs. While these systems are currently sufficiently visualized *statically, in a resting state* using scanning electron microscopy (SEM), an optical inspection capability can provide the *dynamic visualization of functioning systems* that is critical to MEMS characterization.

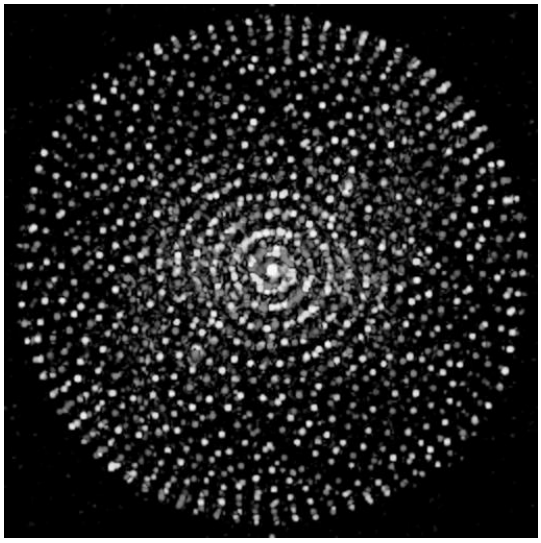

Figure 37: Processed data from the setup in Figure 36.

- Order-of-magnitude **improvements in field of view,** useful for measuring large fields of devices such as large MEMS arrays, and
- Order-of-magnitude **improvements in working distance,** useful for in-situ process monitoring.

3.4 Matisse

In collaboration with the Center for National Research Initiatives (CNRI), the University of California at Berkeley (Berkeley), Carnegie Mellon University (CMU), Lawrence Berkeley National Laboratory (LBNL), and Sarnoff Corporation, we launced the Matisse project to apply next-generation internet (NGI) technology to aid developers of MEMS. The goal is to build and demonstrate a distributed software system that takes advantage of multiple, remote capabilities as if they were available locally. Such capabilities include data sourcing systems, e.g., computer microvision data acquisition, which produces large volumes of imagery; an archival system which supports high-performance i/o; and a computational server capable of processing large amounts of data with complex analysis or visualization algorithms, e.g., computer microvision data analysis and visualization.

Such individual components exist or are being developed and deployed in various locations, principally in advanced research laboratories. However, there are barriers to access to other researchers and to the wider MEMS community, such as the physical location of the systems, the presence of customized interfaces requiring additional implementation-specific expertise, and even the lack of knowledge of the existence or applicability of such systems to users' specific tasks. In the Matisse program, researchers are jointly developing a flexible architecture to enable the use of multiple, remote resources in a seamless, integrated fashion.

The Matisse program currently includes the following collaborators and facilities (Figure 38):

- Corporation for National Research Initiatives (CNRI) Remote Microscope, a scientific grade optical microscope with the capability of being driven by a remote user via a network interface; several such microscopes are to be placed at MEMS fabrication houses under a separate DARPA program [PI: Michael Huff];
- MIT Computer Microvision systems to be deployed and made available at MIT, UC Berkeley, and CMU;
- Sarnoff Corporation X-Ray Micro-Imaging facility for the study of structure and motion in micron-scale structures and devices at Brookhaven National Labs (Long Island, NY);
- Lawrence Berkeley National Laboratories Distributed Parallel Storage System (DPSS), a large scale data cache. Multiple such systems will be used at various geographical locations.

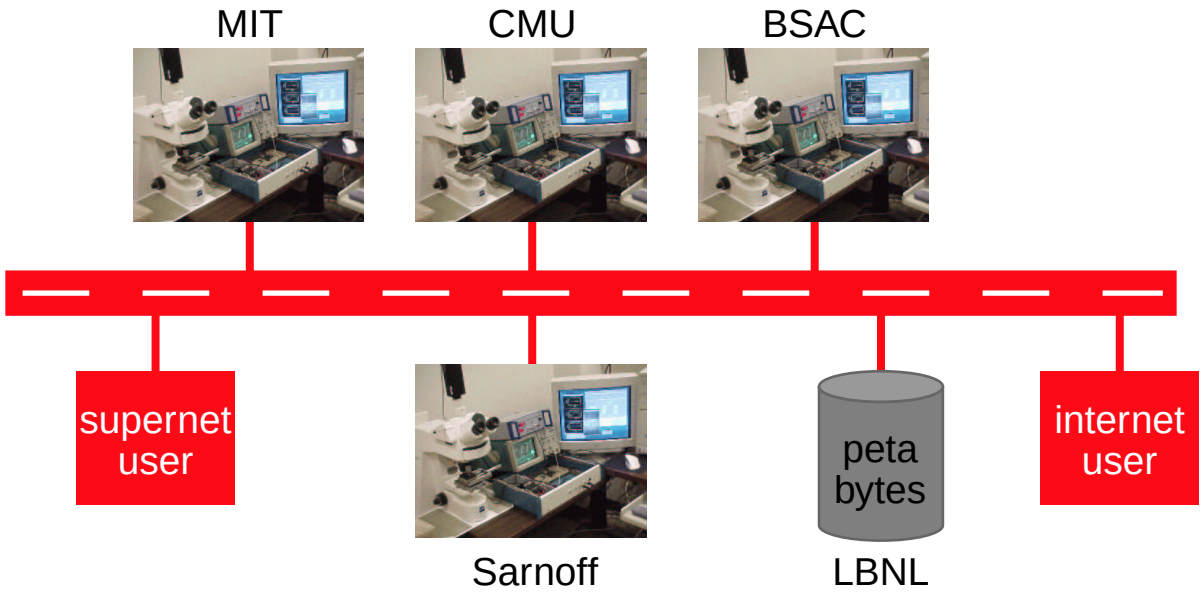

Figure 38: Network of Computer Microvision measurement sites.

3.5 Envisioning MEMS, A Communications Initiative

Under the direction of Felice Frankel, The Envisioning MEMS effort has created a high-end animation (See labeled CD: ENVISIONING MEMS) to communicate the complexity and importance of MEMS fabrication in a clear, concise, and compelling fashion.

We believe the enclosed final animation, ”Envisioning MEMS” represents standards in visualization techniques and aesthetics that are unusual for the research community. Our emphasis was to make the information accessible and accurate, therefore, our time-frame became extended further than initially anticipated, with no-cost extensions. It should be noted that salaries of all participants were paid only for one year, and that all personnel involved spent a full year on the project with no financial compensation.

We propose that this animation be duplicated and distributed to all PI’s in the MEMS community, to the media and administrative assistants in Congress. We also suggest that it be posted on the DARPA/MEMS website. In addition, we encourage MEMS researchers to use this animation or parts of it:

- as an introduction to their own presentations,
- as a component of PI’s websites,
- as a looping animation in research lobbies and corridors,
- for recruitment sessions,
- for other venues (local science museums, schools fairs, teachers workshops) as a means of capturing the attention of the public, students, and young researchers.

(Please note: voice over may be muted and parts may be extracted.)

The following pages are only a few examples of the hundreds of images needed to produce the final animation. These, movies and many other still frames can be found on SUPPLEMENT MATERIAL CD’S 1-4. We encourage the use of these images and clips for web postings and other printed material.

Effort sponsored by the Defense Advanced Research Projects Agency (DARPA) and Rome Laboratory, Air Force Material Command, USAF, under agreement number F30602-97-2-0106. The US Government is authorized to reproduce and distribute for Governmental purposes notwithstanding any copyright notice annotation thereon.

The views and conclusions contained herein are those of the authors and should not be interpreted as necessarily representing the official policies or endorsements, either expressed or implied, of the Defense Advanced Research Projects Agency (DARPA), Rome Laboratory, or the US Government.” ”Cooperative Agreement between The United States of America, U.S. Air Force, Air Force Materiel Command, Air Force Research Laboratory/PKPF, 26 Electronic Parkway, Rome, NY 13441.

*Please note, final report includes 5 CDs. CD labeled Envisioning MEMS is final animation. Remaining 4 CD’s are labeled ”Supplemental Material”. Total files: about 3 Gigabytes.

Figure 39. Selected Images from supplemental discs

The following pages show selected images from enclosed supplemental discs

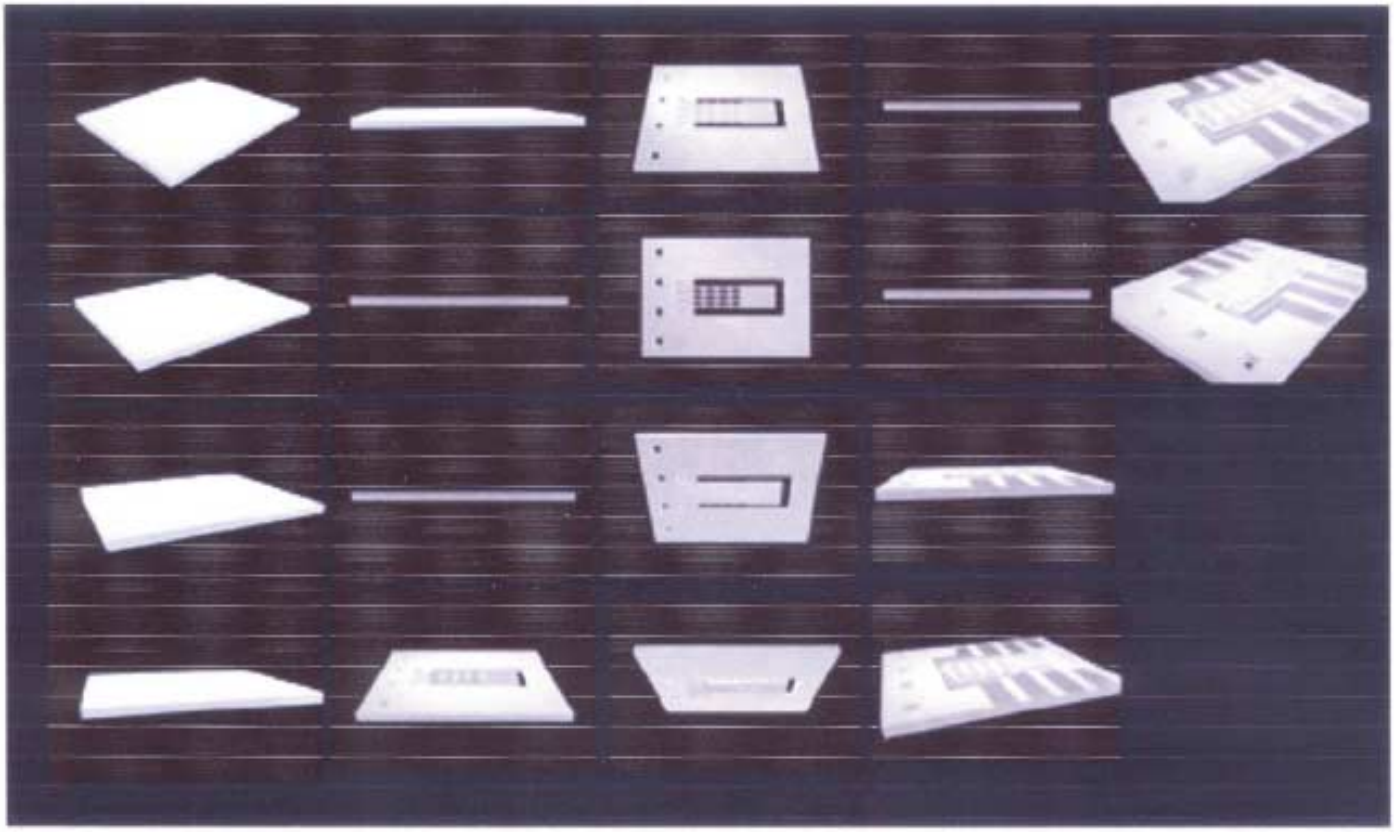

Figure 40. More selected images from supplemental discs

Figure 41. More selected images from supplemental discs

start 01.tif start 02.tif start 03.tif start 04.tif start 05.tif

start 06.tif start 07.tif start 08.tif start 09.tif start 10.tif

start 11.tif start 12.tif start 13.tif start 14.tif start 15.tif

start 16.tif start 17.tif start 18.tif start 19.tif start 20.tif

start 21.tif start 22.tif start 23.tif start 24.tif start 25.tif

start 26.tif start 27.tif start 28.tif start 29.tif start 30.tif

Figure 42: More selected images from supplemental discs

The following two pages show the initial storyboard for the animation, Aug. 2002.
Final version was changed.

Major parts of the animation will be shown in the left two-thirds of the screen, which also will contain compositing and floating windows and text to emphasize specific details. The right third of the screen will have complementary text and composited still images to correspond to and enhance the technical explanations.

sequence

1 manufacturing

Show that etching has been in use for several hundred years. As an example, show a closeup of a portion of a dollar bill. Fade to a closeup CAD representation of the MEM. CAD linework creating a mems layer which then fades to a silicon layer.

Closeup of wafer to show steps in etching and constructing layers. Compositing and coordination with text on right will provide a concise narrative of key events in the MEMS construction process.

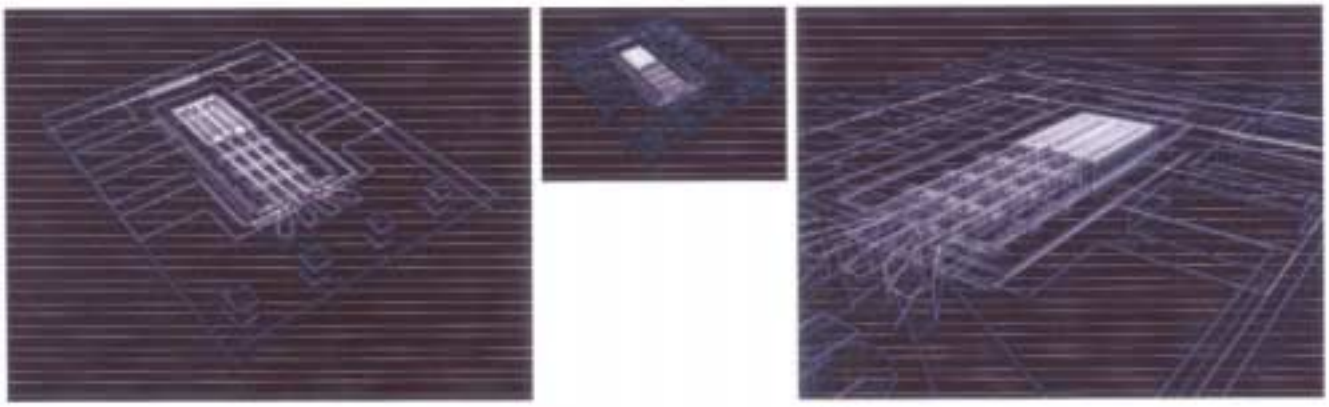

Figure 43. Animation sequence images - manufacturing

2 elements

Complete overview of MEM, each layer will start in an exploded view and as each is identified the animation will sandwich the MEM together. The overall composition will be identified, tubes, packaging, and the camera will focus in on and identify the fuel chamber.

Figure 44. Animation sequence images - elements

3

reaction

Focus on the completed MEM and zoom in on the fuel processor, show how fuel (hydrogen) is catalytically generated from ammonia in the channel of the device. Fuel processor will show that it is first heated (butane) in the left chamber and that the second reaction occurs in the right chamber (ammonia cracked into hydrogen).

Figure 45. Animation sequence images - reaction

4

use

Show the fuel processor placed into an intended device such as a laptop or cellphone.

Publications

Timoner, S. J., and D. M. Freeman, “Multi-Image Gradient-Based Algorithms for Motion Estimation,” Optical Engineering 40: 2003-2016, 2001.

Freeman, D. M., A. J. Aranyosi, M. J. Gordon, and S. S. Hong, “Multidimensional motion analysis of MEMS using computer microvision,” 1998 Solid-State Sensor and Actuator Workshop, June 8-11, 1998, 150-155.

Freeman, D. M. and C. Q. Davis, “Using video microscopy to characterize micromechanical systems,” invided paper, IEEE/LEOS Summer Topical Meeting, Optical MEMS, Monterey CA, July 20-22, 1998, 9-10.

Hemmert, W., M. S. Mermelstein, and D. M. Freeman, “Nanometer resolution of three-dimensional motions using video interference microscopy,” paper and poster at Twelfth IEEE International Conference on Micro Electro Mechanical Systems (MEMS ’99), Orlando, Fl, January 17-21, 1999, 302-308.

D. M. Freeman, “Computer Microvision for MEMS”, invited paper, in ”Material Science of Microelectromechanical Systems (MEMS) Devices II,” M. de Boer, A. Heuer, S. Jacobs, and E. Peeters, editors, Mat. Res. Soc. Symp. Proc. Vol. 605, 151-162, 2000.

Desai, S. P., and D. M. Freeman, “Nanometer Resolution of Three- Dimensional Motion using Mirau Interferometric Optics,” accepted for presentation at International iMEMS Workshop 2001, July 4-6, 2001, NUS, Singapore.

Freeman, D. M., “Measuring Motions of MEMS,” MRS Bulletin, 26: 305-306, April, 2001.

*****References

[1] S. B. Brown, W. Van Arsdell, and C. L. Muhlstein. Materials reliability in MEMS devices. In *Transducers ’97,* pages 591–593. 1997 International conference on Solid-State Sensors and Actuators, Chicago, June 1997.

[2] C. Q. Davis and D. M. Freeman. Statistics of subpixel registration algorithms based on spatio-temporal gradients or block matching. *Optical Engineering*, pages 1290–1298, 1998.

[3] C. Q. Davis and D. M. Freeman. Using a light microscope to measure motions with nanometer accuracy. *Optical Engineering,* pages 1299–1304, 1998.

[4] J. W. Goodman. *Introduction to Fourier Optics*. McGraw-Hill Book Company, New York, 1968.

[5] W. Hemmert, M. S. Mermelstein, and D. M. Freeman. Nanometer resolution of three-dimensional motions using video interference microscopy. In *MEMS ’99: Twelfth IEEE*

International Conference on Micro Electro Mechanical Systems, Orlando, FL, January 1999. IEEE.

[6] H. H. Hopkins and P. M. Barham. The influence of the condenser on microscopic resolution. *Proc. Phys. Soc.*, 63:737–744, 1950.

[7] Shinya Inoué. *Video Microscopy*. Plenum Press, New York, NY, 1986.

[8] Z. Z. Karu. *Fast subpixel registration of 3-D images*. PhD thesis, Massachusetts Institute of Technology, 1997.